Coupling photochemistry with haze formation in Titan's atmosphere, Part II: Results and validation with Cassini/Huygens data

P.P. Lavvas[a,c], A. Coustenis[b], I.M. Vardavas[a,c],*

[a]*Department of Physics, University of Crete, Vassilika Voutes, P.O. Box 2208, 71003 Heraklion, Crete, Greece*
[b]*Observatory of Paris at Meudon, 5 Place J. Janssen, 92195 Meudon Cedex, France*
[c]*Foundation for Research and Technology Hellas (FORTH), Heraklion, Crete, Greece*

Abstract

The new one-dimensional radiative–convective/photochemical/microphysical model described in Part I is applied to the study of Titan's atmospheric processes that lead to haze formation. Our model generates the haze structure from the gaseous species photochemistry. Model results are presented for the species vertical concentration profiles, haze formation and its radiative properties, vertical temperature/density profiles and geometric albedo. These are validated against Cassini/Huygens observations and other ground-based and space-borne measurements. The model reproduces well most of the latest measurements from the Cassini/Huygens instruments for the chemical composition of Titan's atmosphere and the vertical profiles of the observed species. For the haze production we have included pathways that are based on pure hydrocarbons, pure nitriles and hydrocarbon/nitrile copolymers. From these, the nitrile and copolymer pathways provide the stronger contribution, in agreement with the results from the ACP instrument, which support the incorporation of nitrogen in the pyrolized haze structures. Our haze model reveals a new second major peak in the vertical profile of haze production rate between 500 and 900 km. This peak is produced by the copolymer family used and has important ramifications for the vertical atmospheric temperature profile and geometric albedo. In particular, the existence of this second peak determines the vertical profile of haze extinction. Our model results have been compared with the DISR retrieved haze extinction profiles and are found to be in very good agreement. We have also incorporated in our model heterogeneous chemistry on the haze particles that converts atomic hydrogen to molecular hydrogen. The resultant H_2 profile is closer to the INMS measurements, while the vertical profile of the diacetylene formed is found to be closer to that of the CIRS profile when this heterogenous chemistry is included.
© 2007 Elsevier Ltd. All rights reserved.

Keywords: Titan; Atmosphere structure and composition; Haze; Temperature

1. Introduction

The new one-dimensional radiative-convective/photochemical/microphysical model described in Part I is applied here to the study of Titan's atmospheric processes and vertical structure. Under the current description, there is a direct coupling between the photochemically produced species in the atmosphere and the formation of the observed haze structure. The pathways used, provide a vertical production profile for the haze monomers based on the profiles of the chemical species described by the photochemistry. The evolution in size and population of the produced particles is determined by their coagulation, while the final radiative properties are defined in relation to laboratory derived estimations for the spectral dependence of their refractive index. Final conclusions about the efficiency of the suggested pathways are derived through validation of the calculated haze vertical extinction profiles, haze column opacity, spectrally resolved geometric albedo, vertical temperature profile and the chemical composition against the observed values.

In the following sections, we start with the description of the photochemistry that provides the vertical profiles of the chemical species, which are used for the production of the

---
*Corresponding author. Department of Physics, University of Crete, Vassilika Voutes, P.O. Box 2208, 71003 Heraklion, Crete, Greece.
   E-mail address: vardavas@iesl.forth.gr (I.M. Vardavas).

haze monomers, based on the suggested pathways. In Section 2, we present the retrieval of the eddy mixing coefficient used in the calculations and then the vertical profiles of the most important hydrocarbons and nitriles. The latter are validated against the latest measurements from the Cassini/Huygens mission and also from previous space and ground-based observations. These species profiles are the result of processes that include chemical loss to haze formation and the interaction of the haze structure on the radiation field and vertical temperature profile. In Section 3, we provide a detailed description of the contribution of each pathway family to the total vertical haze-production profile. In addition, we discuss the impact of GCR (galactic cosmic rays) on the haze-production profile and the interaction between haze production and chemical composition. The model haze opacity along with its vertical structure define the haze radiative properties, which are controlled by the micro-physical processes. In Section 4, the haze extinction profiles at various wavelengths are compared with those retrieved by the DISR instrument on board the Huygens probe, and further validated by the agreement between the model and measured geometric albedo. In Section 5, the model atmospheric temperature and mass density structures, which depend on the calculated haze structure and chemical composition, are validated against the observed profiles. Sections 6 and 7 present the discussion and conclusions of our study, respectively.

2. Photochemistry

We shall first present the results of the photochemical modelling because they provide the basis for the description of the haze-formation pathways. The species vertical profiles that will be presented in turn implicitly include the effects of the haze structure on the radiation field and the temperature structure. The calculated spectrally resolved geometric albedo that corresponds to the radiation field generating the species vertical profiles presented hereafter and the corresponding vertical temperature profile, are discussed in the following sections. Upper atmospheric neutral abundances were retrieved from neutral (Waite et al., 2005) and ion (Vuitton et al. 2006a, b) spectra of the INMS instrument, while stratospheric vertical profiles and abundances were retrieved from the CIRS limb (Vinatier et al., 2006) and nadir (Coustenis et al., 2007) spectra, respectively. In addition, ground-based observations for some of the nitrile species from Marten et al. (2002) are presented.

2.1. Eddy mixing profile

One-dimensional photochemical models, rely on the eddy mixing coefficient for the inclusion of turbulent diffusion effects on the simulated species vertical distribution. This parameter is usually derived by fitting the measured profiles of species whose vertical structure is controlled only by transportation (inert species). Previous photochemical models have used methane (CH_4) and hydrogen cyanide (HCN) for this purpose. This of course does not mean that these species are inert; after all the complex chemistry of Titan's atmosphere is initiated from methane photodissociation. Their characteristic time for transportation in some regions of the atmosphere is considerably smaller than the characteristic times of photochemical variation and this allows the use of the above molecules as mixing tracers.

Methane is expected to become diffusively separated in the upper atmosphere, above the homopause, while in the lower atmosphere, above the tropopause, its mole fraction is constant and hence no conclusions about the effects of turbulence can be retrieved from there. On the other hand, HCN is produced in the upper atmosphere and as it settles towards the surface, its chemical lifetime increases compared to the diffusion characteristic time, due to its low reactivity with other species. Hence, in previous works, the CH_4 vertical profile and the location of the homopause and slope of its increase due to diffusive separation was used to retrieve information on the extent of turbulent mixing in the thermosphere, while HCN was used for the determination of the mixing in the lower atmosphere.

After the success of the Cassini/Huygens mission, the above approach has become equivocal. Methane's abundance in the upper atmosphere has been measured by Cassini, putting an end to the controversy originating from the initially retrieved value by the Voyager UVS observations (Smith et al., 1982) and their later re-analysis by Vervack et al. (2004). The analysis of the INMS measurements (Waite et al., 2005; Yelle et al., 2006), showed that methane's mole fraction is $2.71 \pm 0.1\%$ at 1174 km. Based on a diffusion model and an isothermal temperature structure they inferred an eddy mixing coefficient of about $4^{+4}_{-3} \times 10^9 \, cm^{-2} \, s^{-1}$, assuming that it is constant in the region between 1200 and 1550 km and that methane does not escape. Yet, allowing methane to escape, the above measured methane mole fraction can be reproduced using a lower eddy mixing coefficient that moves the location of the homopause to lower altitudes (Yelle et al., 2005, 2006).

As was shown by Vinatier et al. (2006), a problem arises if a single mixing profile is used to fit the vertical distributions of HCN and C_2H_6. The modelling of the HCN profile requires the use of strong eddy mixing in the lower atmosphere, which when applied leads to the rapid destruction of ethane. This occurs because the large downward fluxes, generated by the strong mixing, rapidly transport C_2H_6 towards the lower stratosphere where it condenses and is irreversibly lost. This problem was initially reported by Lara et al. (1996), who also found difficulties in matching at the same time the HCN profile and the C_2H_x hydrocarbons with a single mixing profile for all species. This led to the conclusion that, possibly, a loss mechanism for HCN is present in the lower atmosphere, efficient enough to constrain the HCN vertical profile without the use of a large eddy mixing coefficient.

From a different point of view, the recent analysis of ion spectra from INMS (Vuitton et al., 2006a) has identified the presence of methyleneimine (CH_2NH) along with other new nitrile species and also provided an abundance measurement for HCN, with a mole fraction of 2×10^{-4} at 1200 km, which is smaller than the abundances given in this region by previous photochemical models. CH_2NH is an intermediate species in HCN production, the photochemical evolution of which has not been followed by previous models. Its inclusion could possibly explain the overestimation of the HCN abundance in the upper atmosphere and also provide a loss mechanism in the lower atmosphere through its polymerization. These issues are addressed in the following paragraphs, describing the results of the photochemistry.

Based on the above discussion, it is evident that there are processes that control the HCN vertical profile, and also the nitrile chemistry in general, that are not clear yet and have to be investigated. Hence, we have decided not to base our eddy mixing profile retrieval on HCN but use it as a secondary validation parameter. In its place we use ethane, which was suggested also by Vinatier et al. (2006). As a saturated hydrocarbon it is characterized by low chemical reactivity, while due to the overlap of its absorption cross section in the UV region with that of methane, its photochemical life time is significantly large. As shown in Fig. 1, where the characteristic times for mixing and photochemical changes are presented, ethane's vertical profile is mainly controlled by mixing below 700 km making it appropriate as a tracer species.

In addition to the above tracers, now we also have information for the mixing in Titan's atmosphere from a really inert species, argon (Ar). INMS (Waite et al., 2005) has detected ^{40}Ar at a $7.1 \pm 0.1 \times 10^{-6}$ mixing ratio in the upper atmosphere, while the GCMS instrument onboard the Huygens probe has given $4.32 \pm 0.1 \times 10^{-5}$ in the lower atmosphere, close to the tropopause (Niemann et al., 2005). Argon's vertical profile is constant since it does not

react with other species in the atmosphere and varies only as it moves into the diffusive separation region. Hence its variation with altitude provides realistic information about the turbulence effects and can set constraints on the minimum and maximum values of eddy mixing in the atmosphere.

The eddy mixing coefficient used in the calculations is presented in Fig. 2 along with the calculated vertical profiles of the above species used for its derivation. Using only argon as a tracer for the atmospheric eddy mixing is not sufficient, because its vertical profile, defined by the above two altitude measurements, can be fitted with different altitude variations of the mixing profile. That is why at least one more tracer species is necessary. In order to keep the simulated ethane vertical profile close to the CIRS observed values, which suggest a rather constant variation with altitude in the region between 200 and 500 km (Vinatier et al., 2006), a strong eddy mixing profile must be considered. In the lower atmosphere, the magnitude of the mixing profile controls the flow of species towards the condensation region. The values of the eddy profile in this region affect the ethane profile, shifting the whole distribution towards larger (smaller) mole fractions for smaller (larger) values of the mixing coefficient. Having this region constrained, the upper atmosphere mixing profile was varied until a good fit to the argon measurement was achieved.

A comparison with the eddy mixing profiles used in previous photochemical models is provided in Fig. 3. It is obvious that the current mixing profile is significantly larger in the lower atmosphere, between 250 and 650 km than the previously suggested profiles in order to constrain the ethane profile to a vertical variation similar to the observed one. Our profile follows very closely the profile suggested by Vinatier et al. (2006) which was calculated based on the CIRS retrieved ethane profile for the region below 500 km. Above this region, our mixing profile is close to the Wilson and Atreya (2004) profile but slightly larger in the upper atmosphere above 1000 km, in order to fit the argon measurement. Between 150 and 250 km, Hourdin et al. (2004) derived an estimate for the eddy mixing profile based on GCM simulations. They suggested a vertical mixing between 10^6 and $5 \times 10^7 \, cm^2 \, s^{-1}$. The lower limit of this range is close to the magnitude of our mixing profile at 250 km but the structure of our profile suggests a rapid decrease of the mixing coefficient at lower altitudes in order to constrain the loss of the species due to condensation. It should be kept in mind that transportation in other directions than the vertical can significantly affect the species profiles and explain the differences in the mixing profiles derived by GCM simulations and one-dimensional models.

The position of the homopause, based on the argon molecular diffusion coefficient (which is very close to that of methane used in previous models) and the calculated vertical temperature profile and number density, is near 900 km, which is close to the 850 km retrieved by Wilson
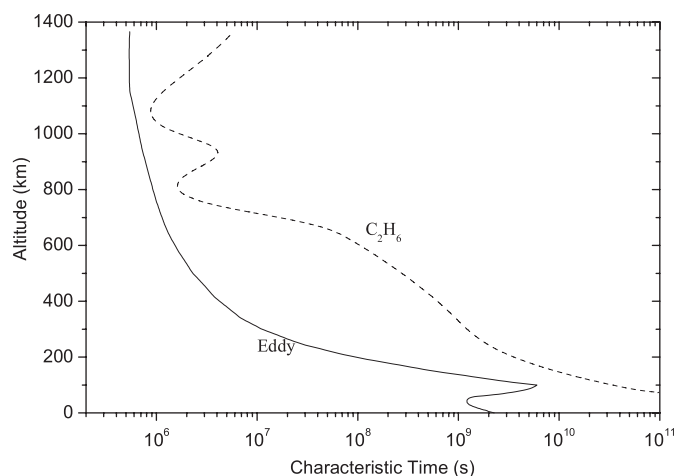

Fig. 1. Characteristic life time of C_2H_6 relative to characteristic time of transport due to eddy mixing.
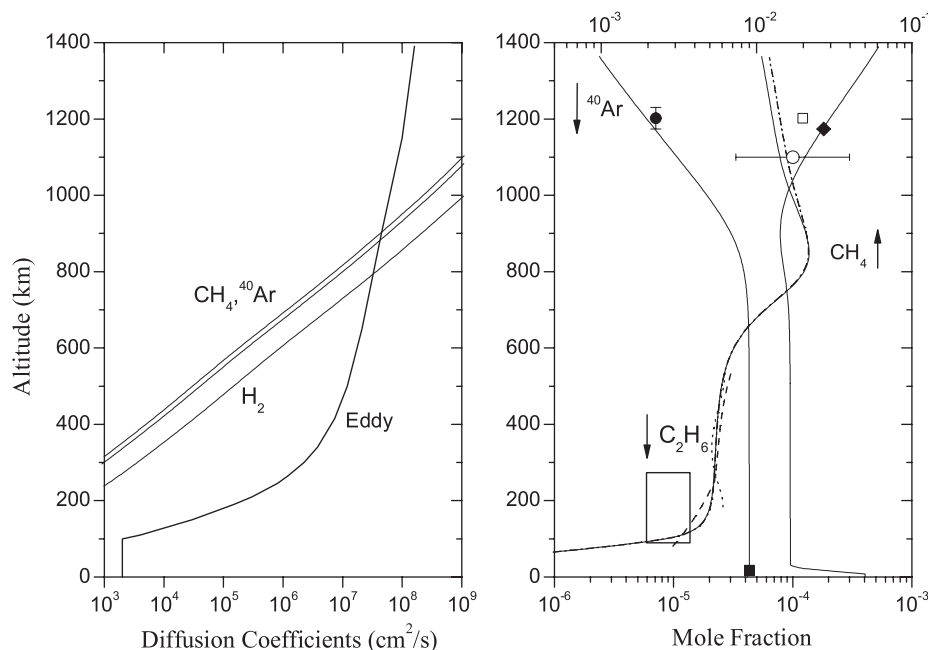
Fig. 2. The retrieval of the eddy diffusion coefficient used in the model calculations. The left panel presents the derived vertical eddy mixing profile that provided the best fit to the calculated vertical profiles of the simulated species, along with the molecular diffusion coefficients for argon, methane and molecular hydrogen. The altitude at which the argon molecular diffusion coefficient intersects the eddy mixing profile, provides an estimation of the region where the homopause is placed. The right panel presents the model calculated vertical profiles of the species used for the retrieval of the mixing profile. The filled cycle and square correspond to the argon measurements from INMS (Waite et al., 2005) and GCMS (Niemann et al., 2005) measurements, respectively. The open square and cycle are the INMS measurements for ethane (Waite et al., 2005; Vuitton et al., 2006a) and the filled diamond is the INMS measurement for methane (Yelle et al., 2006). The box represents the CIRS-retrieved range of abundances for C_2H_6 at 33°N (Coustenis et al., 2007) and the dashed and dotted lines correspond to the CIRS-inferred profiles of ethane at 15°S and 80°N, respectively (Vinatier et al., 2006). Solid lines correspond to the model results, while the dashed-dotted line represents the sensitivity of the model ethane profile to the N_2 dissociative photoionization scheme. Arrows indicate the axis used for each species (bottom for ethane and argon and top for methane).
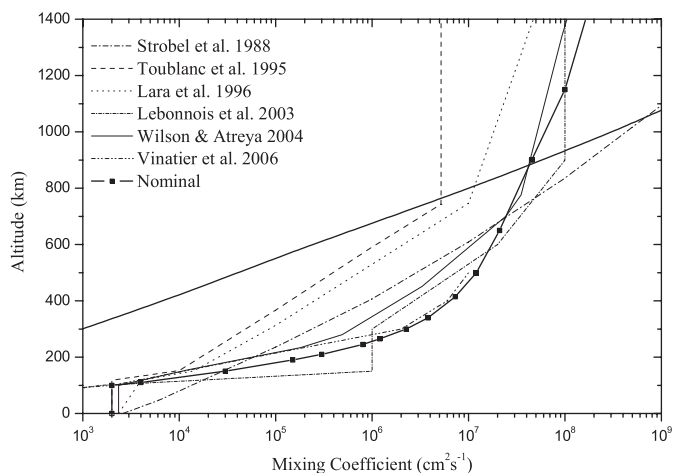

Fig. 3. Eddy diffusion profiles used in previous photochemical models. The solid line traversing all mixing profiles is the methane diffusion coefficient.

and Atreya (2004). Apart from the use of different photochemical schemes and reaction rates, the variability observed between previous photochemical models for the shape of the mixing profile and the position of the homopause, is related to the fact that the methane stratospheric abundance was not well constrained at that

time but varied significantly among different simulations, while the thermospheric abundance was overestimated. Now, from the Cassini/Huygens mission there are significantly better constraints for the methane profile, as discussed in Part I.

In addition, it becomes apparent that in order to provide a match to the INMS measured methane abundance in the upper atmosphere (Yelle et al., 2006), a strong eddy coefficient cannot be applied, since this would lead to a large overestimation of the argon profile. This leaves us with the second choice, that of methane escape. In the profile presented in Fig. 2 methane was allowed to escape from the top of the simulated atmosphere with a flux equal to 70% of the diffusive flux at that level, with the latter reaching at these altitudes its diffusion limited value. Under this condition the simulated methane mole fraction is very close to the observed one.

2.2. Chemical composition—validation with Cassini/Huygens

The model vertical profiles for the main hydrocarbons, and nitriles are described in the following paragraphs and compared with the measurements of the instruments on board Cassini. Before comparing them with the observations, it is important to note that we solve for a solar zenith

angle of 60°, which corresponds to mid-latitude conditions, so that our profiles should, in principle, lie between the equatorial and northern vertical profiles retrieved from CIRS limb spectra (Vinatier et al., 2006). The polar profiles are affected by the downwelling of air masses, i.e. the Hadley cell. The subsiding cell at the winter North pole, enhances the transportation of species formed in the upper atmosphere towards the lower layers, which explains the latitudinal variations observed. Such a process is not described under the one-dimensional character of our simulation. We furthermore compare with the 33°N values of the CIRS retrieved stratospheric abundances from nadir spectra (Coustenis et al., 2007), which represent mid-latitude conditions (keeping in mind the large obliquity of Titan's rotational axis, 27°). In addition, it must be noted that the INMS derived abundances correspond to a specific flyby (T5) that represents a specific location and solar illumination conditions on Titan's disk. Although the atmosphere at the probed altitudes is expected to be well mixed (due to the observed super-rotation of the atmosphere and also suggested by the convergence of the vertical temperature profiles from different latitudes above 400 km—see Section 5), possible variations cannot be excluded when comparing the global average results of the model with the local observations. Unless stated otherwise, the upper atmosphere will correspond to the INMS probed altitude region (thermosphere), while the lower atmosphere corresponds to the CIRS probed region (stratosphere).

2.2.1. Hydrocarbons

C_2H_6: Ethane production is dominated by the methyl radical (CH_3) recombination rate. This is a pressure-dependent reaction and the rate used in the model description for the low-pressure limit has a major impact, not only to the final ethane profile in the upper atmosphere, but also to the profiles of ethylene, acetylene and methane. This happens because the methyl radical is related to the formation of all C_2H_x species. The efficiency of the recombination reaction at low pressures, controls the population of methyl radicals that are available for the production of ethylene through reaction with excited methylene:

$$^1CH_2 + CH_3 \rightarrow C_2H_4 + H$$
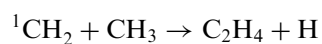
while the photolysis of ethylene is the main production pathway for acetylene in the upper atmosphere. Hence, the efficiency of recombination at low pressures controls the relative magnitudes of acetylene and ethane. In addition, CH_3 radical photolysis at 216 nm, is a significant source of excited methylene radicals:

$$CH_3 + hv \rightarrow {}^1CH_2 + H$$
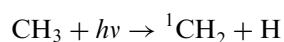
that enhances methane's catalytic destruction and hence affects the production of all hydrocarbons.

The importance of methyl photolysis was originally noted by Yung et al. (1984) and included in all photochemical models for Titan's atmosphere since then. The absorption cross section used is the one in a very narrow region around 216 nm, which has been reported over a large range of temperatures. For room temperature, which is the lowest temperature we found in the literature, we used the Adachi et al. (1980) high resolution measurements that cover the 215.3–217.1 nm region. It is important to note the strong temperature dependence of the cross section (with increasing absorptivity for decreasing temperature) that can be readily seen if these cross sections are compared with the Zalicki et al. (1995) high resolution cross sections reported for the same spectral region but at 1600 K. Previous models have included the photolysis of CH_3 in this region but used the cross section of Parkes et al. (1973).

The Callear and Metcalfe (1976) measurements have shown that the electronic transitions in this region overlay a continuum, which extends down to 204 nm and although it is of a smaller cross section, it could also contribute to the total photodissociation due to its broad character. Absorption peaks have also been observed around 150 nm (Pilling et al., 1971). Photolysis at these wavelengths follow a different pathway giving (Kassner and Stuhl, 1994)

$$CH_3 + hv \rightarrow CH + H_2.$$
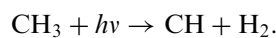
Due to the significant role of CH_3 in Titan's photochemistry, it is important to have a better understanding of its absorption spectrum, which at the moment does not exist. In the current calculations we have included along with the 216 nm absorption feature, the absorption cross sections at 150 nm but not the absorption continuum reported in the region between 204 and 216 nm, since there are no clear measurements.

For the methyl recombination rate, laboratory measurements have provided some results for the high-pressure limit rate over a range of temperatures, with most recent, the results of Cody et al. (2003), which were obtained for low temperature conditions, appropriate to Titan. The low-pressure limit is difficult to measure and the contribution of theoretical descriptions based on measurements at the fall-off region and at the high-pressure limit, was necessary in order to retrieve a rate. The suggested rates found in the literature depend also on the bath gas responsible for the deactivation of the energized complex, which is usually taken to be one of either H_2, He, Ar or N_2. The extrapolation though, of the suggested low-pressure limit rates to Titan's conditions leads to results that can vary by orders of magnitude and hence produce significantly different C_2H_6 profiles.

In the current calculations we have used the high and low pressure rate limits given in the Cody et al. (2003) work. Although the latter have used He as a bath gas, which could lead to smaller rates compared to those for N_2, we have used their results since they are the only ones published for low temperature conditions. A correction to the rate due to the N_2 bath in Titan's atmosphere can be performed through the theoretical estimation of Smith

(2003) who calculated the ratio of the low pressure limits due to different bath gases. For the case of He and N_2 the ratio is $k_0(N_2)/k_0(He) = 1.714$ although this, in general, is temperature dependent. Nevertheless using this low pressure limit for the methyl recombination produces an ethane profile that is significantly lower than what is observed. The same has been noticed by Wilson and Atreya (2004) who multiplied their low pressure limit (they used the low pressure limit rate suggested by Slagle et al., 1988, which is of similar magnitude with the Cody et al., 2003 rate) by a factor of 10. This is also suggested by ISO observations of CH_3 on Saturn (Bézard et al., 1998; Atreya et al., 1999). In view of these results we have also adopted this conclusion of under-estimation for the low pressure limit of methyl recombination and multiplied the above rate by 10. The model profile for ethane, with the above described rate, has been presented in Fig. 2. In the upper atmosphere, the calculated mole fraction at 1200 km is 6.8×10^{-5} compared to the 1.2×10^{-4} retrieved by the INMS neutral spectra (Waite et al., 2005) and within the range reported based on the INMS neutral spectra from Vuitton et al. (2006a). When the N_2 dissociative ionization is assumed to yield ground state nitrogen atoms, as was done in previous models, the loss of ethane is decreased and its mole fraction at the same altitude increases to 7.8×10^{-4} (see dash-dotted line in Fig. 2).

C_2H_4: Ethylene has been a source of surprise in photochemical models, due to the low abundance predicted by them in the lower atmosphere, compared to the observed one. Voyager's IRIS measurements have placed the stratospheric C_2H_4 mole fraction at 1.5×10^{-7} at the equator, increasing up to 1.5×10^{-6} at the winter pole (North at that time), while ISO retrieved a disk average value of 1.2×10^{-7} (Coustenis et al., 2003). The above values are in agreement with the mid-latitude mole fraction of 1.5×10^{-7} retrieved by CIRS nadir spectra (Coustenis et al., 2007), although this time there is a hint for a reversed latitudinal variation. The latest results from the limb spectra (Vinatier et al., 2006) have shown that ethylene's vertical profile increases monotonically below 300 km, with the difference of the two latitude profiles becoming smaller towards the surface. From previous works, only Lara et al. (1996) provided a vertical profile which matched the observed stratospheric abundance, by forcing the surface mole fraction to a fixed value, which is equivalent to assuming a surface emission of C_2H_4. Our model simulation, suffers from the same low estimation of the ethylene abundance (Fig. 4a) although it provides a mole fraction in the upper atmosphere which is in close agreement with the INMS retrieved one (Vuitton et al., 2006b).

The loss processes for ethylene in the lower atmosphere are dominated by photolysis and reaction with atomic hydrogen leading to the formation of the ethyl radical (C_2H_3). Recent results from two-dimensional photochemical models and GCMs have provided a possible solution for this underestimation, by suggesting that the enhancement of ethylene could be due to circulation effects
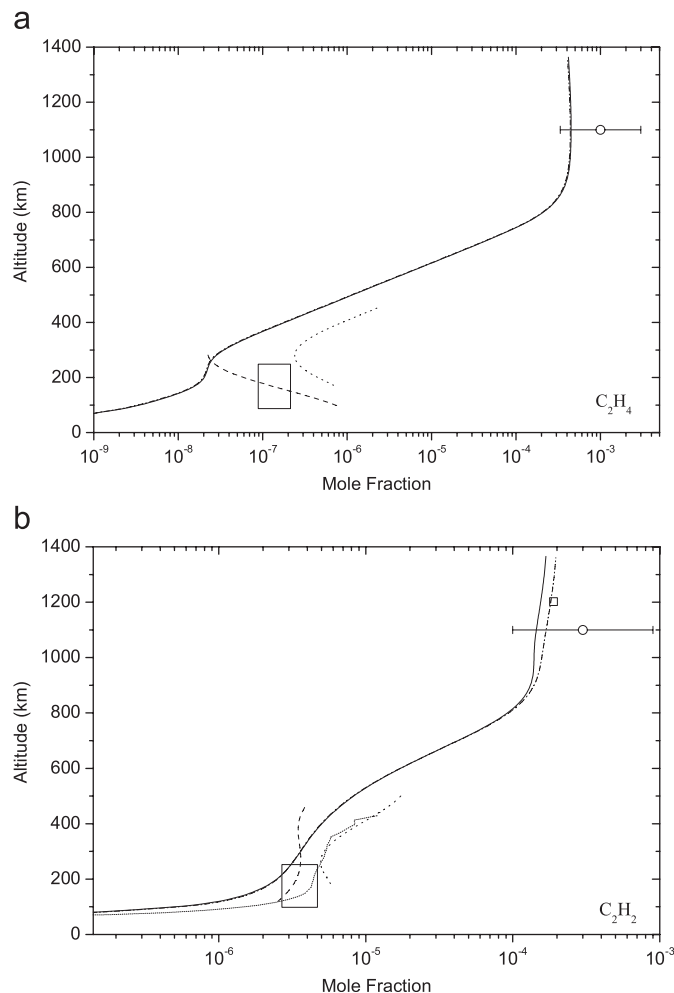

Fig. 4. Model results for the mixing ratio of ethylene: (a) and acetylene (b) in Titan's atmosphere and comparison with the latest measurements from the Cassini/Huygens mission. Solid lines correspond to model results, dashed and dotted lines correspond to the CIRS retrieved profiles for 15°S and 80°N, respectively (Vinatier et al., 2006) based on limb spectra, while open squares and circles represent the INMS measurements for the upper atmosphere from Waite et al. 2005 and Vuitton et al. 2006a, b, respectively. CIRS abundances from nadir spectra at 33°N are also shown in boxes (Coustenis et al., 2007) and the short-dotted line corresponds to the Hourdin et al. (2004) acetylene profile generated by a two-dimensional photochemical/dynamical model that was found to provide a good fit to the CIRS nadir spectra for the equator. The dash-dotted line presents the sensitivity of the model to the N_2 dissociative ionization scheme.

(S. Lebonnois, personal communication). The downwelling flux of C_2H_4 due to the Hadley cell circulation, could lead to an enhancement in the lower atmosphere, since ethylene does not condense at the low temperature conditions found in this part of Titan's atmosphere, while most of the other species do condense. In view of the relatively good agreement of our model and that of previous models with measurements regarding the other hydrocarbons in this region, the dynamical solution seems to be a possible scenario. Whether this process can account for the total abundance of ethylene in the lower atmosphere or there is a need for photochemical adjustments to obtain

an abundance comparable with the observed one, is something which must be tested by future simulations.

C_2H_2: Acetylene's vertical profile is presented in Fig. 4b. The simulated profile is close to the upper atmosphere retrieved abundance by INMS (Waite et al., 2005; Vuitton et al., 2006a). The structure observed in this region, with the small minimum at about 1100 km is related to the N_2 photolysis scheme and the reaction of the produced $N(^2D)$ atoms with acetylene. The new scheme used in the current calculations regarding the products of the N_2 photodissociative ionization, increases the production of excited nitrogen atoms and enhances their role in the destruction of hydrocarbons in the upper atmosphere. The scheme used in previous models, where only $N(^4S)$ atoms are formed yields the dash-dotted line in Fig. 4b.

In the mesosphere, the model results provide a reasonable profile which is in between the equatorial and polar vertical profiles retrieved by CIRS (Vinatier et al., 2006). Only in the lower atmosphere, below 300 km do our results underestimate the acetylene abundance. At 200 km the calculated abundance is smaller by a factor of 1.33 and 1.48 from the CIRS equatorial value and mid-latitude value (Coustenis et al., 2007), respectively. Due to the broad pressure-range probed by the ν_5 band of acetylene, the latter authors managed to retrieve information about the vertical structure of its profile from the CIRS nadir spectra. They concluded that the vertical profile generated through the two-dimensional photochemical–dynamical model of Hourdin et al. (2004) (see description in Coustenis et al., 2007 and short-dotted line in Fig. 4b) provided the best fit to the observed spectra relative to previous photochemical results. Although our profile gives a similar altitude variation with their suggested profile above 250 km, it decreases faster at lower altitudes. The observed difference could be corrected by adjusting the mixing efficiency in the lower stratosphere, but such a treatment would lead to an increase in other hydrocarbons and nitriles in this region that are well simulated by the current eddy mixing profile. Further, decreasing the eddy mixing in the mesosphere provides an acetylene profile which is closer to the CIRS observed one, but in this way the fit to C_2H_6 and Ar that are used as tracers, is destroyed. Possibly, dynamical effects are able to adjust the acetylene mole fraction closer to the observed one.

C_3H_4: Methylacetylene (CH_3C_2H) and its isomer allene (CH_2CCH_2) are presented in Fig. 5a. INMS (Waite et al., 2005) has provided a mole fraction of $3.86 \pm 0.22 \times 10^{-6}$ for the C_3H_4 mass channel, a value close to that of the model profile for the combined contribution (2.7×10^{-6}). Allene is converted to methylacetylene in the presence of atomic hydrogen, as described in Part I, which explains its decrease relative to the CH_3C_2H abundance as we move towards lower altitudes. Yet, in the lower atmosphere the CH_3C_2H profile is underestimated compared to the CIRS lower limit retrieved abundance for the equator (Vinatier et al., 2006) and the CIRS mid-latitude abundance (Coustenis et al., 2007). At 300 km our profile is five times smaller than

the equatorial value and also it presents a vertical structure significantly different from the observed one. Previous photochemical models also tend to underestimate the methylacetylene abundance relative to that observed by CIRS, with the exception of Toublanc et al. (1995) although this is probably related to their use of a significantly smaller eddy mixing coefficient (see Fig. 3) rather than due to differences in the photochemical scheme.

The possible reasons for this underestimation are open to discussion. The main loss mechanisms for methylacetylene are photolysis and the three body reaction with atomic hydrogen that leads to the production of C_3H_5. From the good agreement between the observed and modelled geometric albedo in the UV region (see Fig. 19), and the structure of our modelled haze extinction profile (Figs. 17 and 18), which is in reasonable agreement with that retrieved by the HASI instrument on board the Huygens probe, the possibility of an enhanced photolysis due to a possible underestimation of the haze or gas opacities, is probably not the answer to our problem. For the hydrogen population, we believe we have a realistic simulation as will become apparent in the discussion for the diacetylene profile later on. Hence the underestimation is probably related to a lack of production in the lower atmosphere. An enhanced production in the lower atmosphere could be related to the local enhancement observed for ethylene but not reproduced by the model calculations. Another possible source for the low abundance of CH_3C_2H could be the overestimation of the propane profile in the lower atmosphere discussed later.

C_3H_8: Propane's production is dominated by the combination reaction between methyl and ethyl radicals. The high-pressure limit rate for this reaction has been measured for elevated temperatures and theoretically investigated for lower ones. Most recent laboratory measurements are those of Sillesen et al. (1993) and Knyazev and Slagle (2001), while previous measurements are reviewed in Tsang and Hampson (1986) and Baulch et al. (1992). The rates measured in these reports, include also the hydrogen abstraction channel:

$$CH_3 + C_2H_5 \rightarrow C_2H_4 + CH_4$$
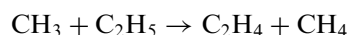
which was not possible to isolate. Theoretical investigations have attempted to provide some information about the relative importance of the two channels and the transition through which they proceed. Zhu et al. (2004) reported rates for the two main energetically possible channels (association/abstraction). Their results are in good agreement with the latest measurements and other theoretical investigations and are those used in the current calculations. Based on these reports, for temperatures below 600 K the reaction rate presents a negative temperature dependence and the association rate appears to be dominant and pressure independent for the measured pressure range (1–21 Torr). This suggests that for Titan, propane production can proceed readily even at low pressures compared to other three-body reactions. For
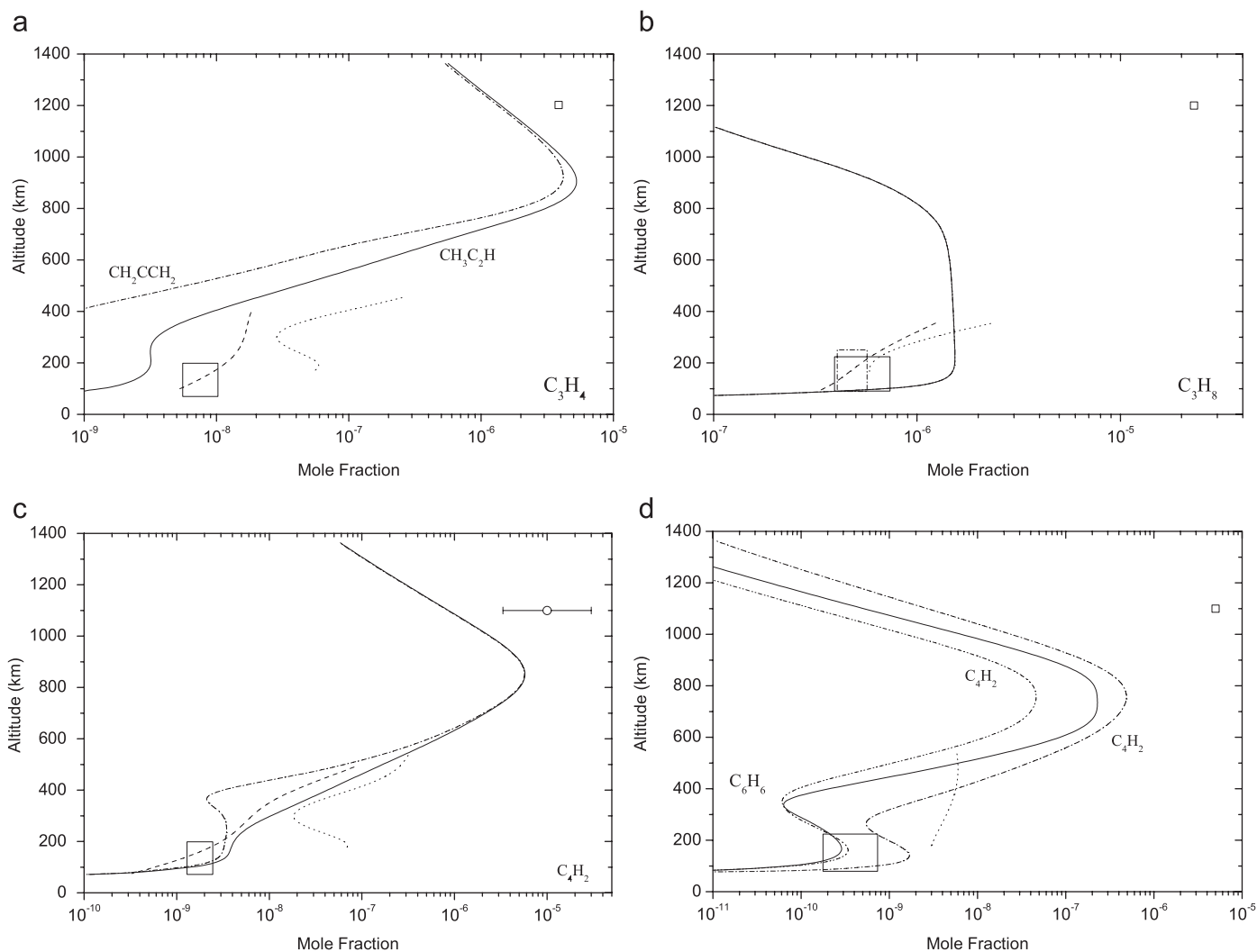
Fig. 5. Model calculated vertical profiles for the mole fractions of important hydrocarbons in Titan's atmosphere together with Cassini/Huygens measurements; the symbols are the same as those used in Fig. 4. In (b) the dashed-dotted box corresponds to the range of values set by the Roe et al. (2003) measurements for the propane stratospheric abundance. In (c) the solid and dashed-dotted lines correspond to model results for diacetylene, with and without the inclusion of the PRM heterogeneous process discussed in the text. In (d) the upper atmosphere measurement corresponds to an upper limit for the benzene abundance retrieved during the first flyby of Cassini. The lines correspond to the model profiles for benzene (solid line), triacetylene (dash-dotted line) and benzyne (dash-double-dotted line).

the low pressure limit we have estimated the rate with that of the methyl radical recombination rate.

The resulting propane profile is significantly different from what is suggested by the observations. In the upper atmosphere the model suggests an abundance that is more than two orders of magnitude smaller than that measured by INMS (Waite et al., 2005). This suggests that other processes, not included in the model, are responsible for the production of propane in the upper atmosphere.

In the lower atmosphere our modelled profile is larger and has a significantly different altitude variation than the CIRS retrieved vertical profiles (Vinatier et al., 2006) and stratospheric abundance (Coustenis et al., 2007). The observed profiles suggest a decreasing abundance with altitude, with the two latitude profiles converging towards the condensation region. In contrast, our model suggests a constant vertical mole fraction, before the abundance starts

to decrease towards the condensation region. In previous photochemical models, Lara et al. (1996) has provided a vertical profile which increased with altitude in the above region similar to the observed altitude variation, while Wilson and Atreya (2004) suggested that the absence of the C_3H_7 radical in the former photochemical model, led to this altitude variation. The recycling induced by the following scheme:

$$C_3H_8 + hv \rightarrow C_3H_6 + H_2,$$

$$H + C_3H_6 + M \rightarrow C_3H_7 + M,$$

$$2\,C_3H_7 \rightarrow C_3H_6 + C_3H_8$$
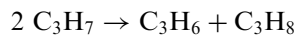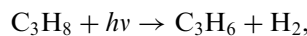
conserves propane and provides the constant mole fraction in the lower atmosphere observed in their model results, as in ours. Hence, one would expect that if this process was

for some reason reduced, then the abundance of C_3H_6 would increase and by its photolysis an enhancement in the methylacetylene profile would be observed. Yet, based on our calculations, removing the above scheme, did not have any significant effect on the structure and abundance of propane or methylacetylene, rendering the above scheme not important in our simulation. The reason for this is that propane's production is dominated by the methyl–ethyl addition reaction in the total vertical range of Titan's atmosphere, with any secondary production mechanisms having a negligible contribution. Since C_3H_8 is not affected, C_3H_6 also remains the same and hence there is no significant change in C_3H_4.

Photochemical loss processes for propane are limited. Due to the overlap of propane's absorption cross section with that of methane, which is present in significantly larger amounts, propane photodissociation is small. On the other hand, as a saturated hydrocarbon it presents limited reactivity with other species, of which the most important is that with C_2H. Hence, its vertical profile is balanced by diffusion and loss to condensation. Reducing the eddy mixing coefficient in the stratosphere - mesosphere, in order to provide a better match, destroys the agreement with ethane and argon, which are used as mixing tracers. Increasing the mixing in the lower atmosphere, below the stratopause, in order to increase the condensation flux, leads to a strong underestimation of ethane and acetylene in the lower atmosphere, since the condensation fluxes of these species (along with all other condensing species) increases also. Hence, we are currently left with the possibility of an enhanced production of propane in the lower atmosphere to explain our model overestimated abundance in this region.

C_4H_2 *and H, H_2*: Diacetylene is an important species because it is directly related to haze production pathways. In addition, since in the lower atmosphere the chemical loss of C_4H_2 is dominated by reaction with atomic hydrogen, the vertical profile of diacetylene can be used as a tracer for the maximum abundance of atomic hydrogen allowed in this part of the atmosphere. INMS (Vuitton et al., 2006b) has measured the upper atmospheric abundance at 1×10^{-5} mole fraction, while the CIRS retrieved vertical profiles have constrained the mole fraction to $\sim 10^{-8}$ in the vicinity of the stratopause (Vinatier et al., 2006). At about 110 km, where the contribution function from nadir spectra for this species peaks at mid-latitudes, CIRS gave a mole fraction of $1.8^{+0.6}_{-0.5} \times 10^{-9}$ (Coustenis et al., 2007). In Fig. 5c the dashed dotted line presents the calculated vertical profile of C_4H_2. It is obvious that in the region of 400 km where the calculated atomic hydrogen abundance presents a broad maximum (see Fig. 6c), C_4H_2 exhibits a significant decrease below the lower limit set by the CIRS equatorial profile (Vinatier et al., 2006), while for higher and lower altitudes the agreement with the observed abundances is better. The vertical profile of diacetylene presents a dependence on the used eddy profile, something which was also reported by Wilson and Atreya (2004). Yet,
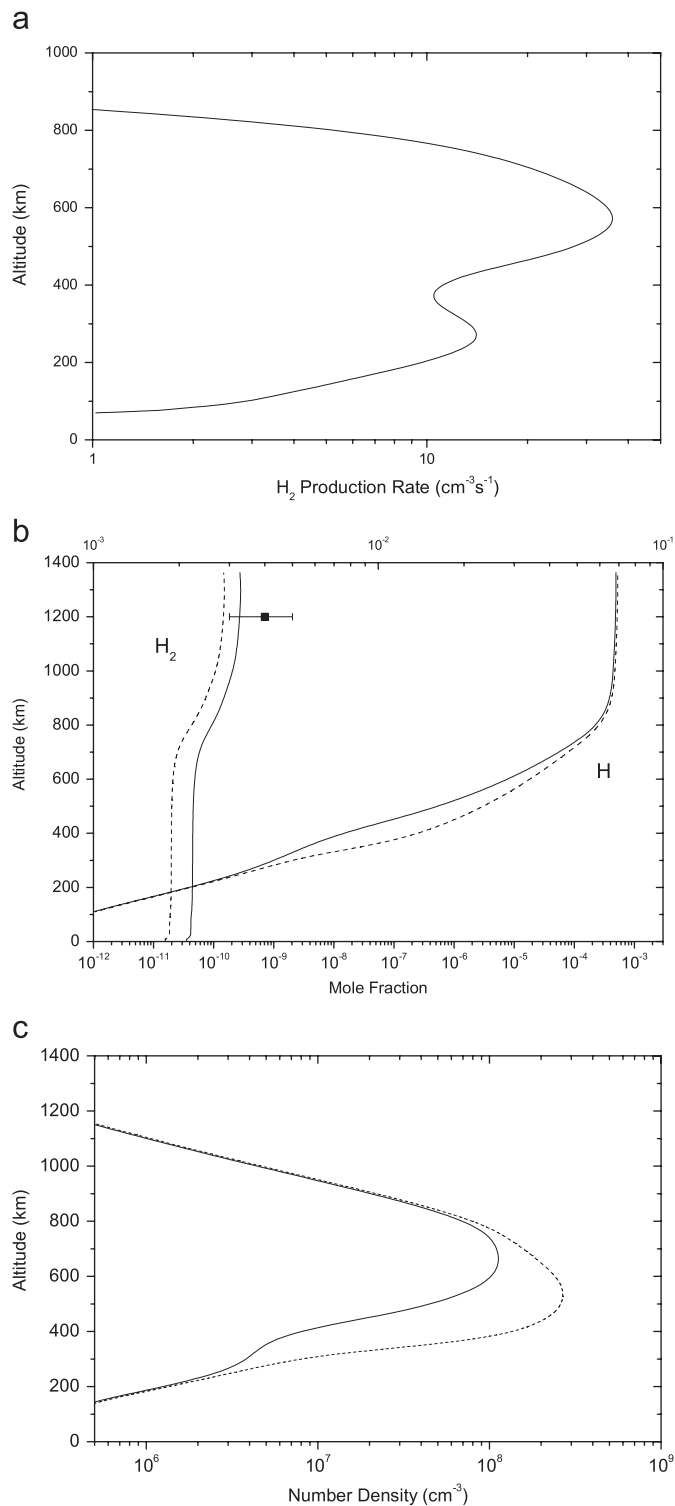
Fig. 6. The effects of heterogeneous transformation of atomic to molecular hydrogen at the surface of the aerosol particles. (a) The calculated production rate of H_2, or equivalently loss rate for atomic H due to this process, has two pronounced peaks related to the number density of atomic hydrogen and size distribution of the aerosol particles (see text). The impact of the PRM process on the resulting mixing ratios of atomic (bottom scale) and molecular hydrogen (top scale) of the model (b) is significant with a decrease in the H abundance between 300 and 800 km, which is more evident when viewed in terms of number density (c), and an increase in the H_2 mole fraction, giving better agreement with the observed abundance in the upper atmosphere from Yelle et al. (2006).

having the mixing profile set with the above described method and assuming a single mixing profile for all gas species, there is not much that can be done by changing the mixing profile in order to correct the C_4H_2 profile, without destroying the fit to the tracers used. At the same time, the calculated H_2 profile (Fig. 6b) is lower than the INMS retrieved abundance in the upper atmosphere (Yelle et al., 2006). These two facts hint at the possibility of an underestimation in the conversion of atomic hydrogen to molecular.

The underestimation of the conversion of H to H_2 was initially noted by Yung et al. (1984) who suggested that heterogeneous processes at the surface of the aerosol particles could possibly enhance this process. Bakes et al. (2003) and Lebonnois et al. (2003) were the first to describe and model this process for Titan's haze particles based on the prompt-reaction model (PRM) of Duley (1996). In this model, atomic hydrogen from the gas medium reacts readily with H atoms that are bonded at the surface of the particles giving H_2, which is released to the atmosphere. They concluded that this was an important process for the H and H_2 abundances, but also for other hydrocarbon species in the stratospheric region. In their calculations, they used the Toon et al. (1992) size distribution for the haze particles and estimated the activation energy for hydrogen abstraction based on the Sugai et al. (1989) measurements, which were performed at room temperature. Recently, Sekine et al. (2006) have reported measurements for the activation energy at low temperatures, appropriate for Titan's conditions and found that the activation barrier for abstraction is significantly smaller than previous estimates, making this process even more efficient. Based on their results, the probability of reaction of atomic hydrogen with the surface of an aerosol particle is given by

$$p_b = 1.9 \times 10^{-3} e^{-300/T}$$

for the temperature range 160–300 K, which means that the cross section for bonded hydrogen abstraction will be given by

$$\sigma_b = 4\pi r^2 p_b$$

with r the radius of the aerosol particle.

We have included this process in our calculations following the description given in Lebonnois et al. (2003) and using the size distribution for the haze particles calculated in our microphysical model, presented in the next section (see Fig. 15). The impact of the process on the vertical profiles is found to be important. The production rate of H_2 molecules and hence loss rate of atomic H, is presented in Fig. 6a. The shape of the profile is different from that shown in Bakes et al. (2003) due to the significant differences between the size and number density profiles used in the two calculations. There are two production peaks observed, which are related to the fact that the production rate is proportional to the number density of atomic hydrogen and to the number density and

surface area of the particles. The upper peak is related to the region where the H number density reaches its maximum value due to production by photochemical processes, while the lower peak comes from the fact that as we move towards the surface the size and hence the surface area of the particles upon which abstraction of H atoms can take place becomes larger due to the coagulation process. At the same time though, larger size particles are present in smaller densities, which explains the decreased contribution of the secondary peak to the overall production rate.

The resulting model atomic hydrogen and molecular hydrogen mole fractions are presented in Fig. 6b. A sharp decrease in the H profile in the region between 300 and 800 km is evident as shown in Fig. 6c in terms of the number density. The molecular hydrogen formed increases the initial abundance calculated by the model and provides a mole fraction in the upper atmosphere that is closer to the one retrieved from the INMS measurements (Yelle et al., 2006). The escaping hydrogen fluxes at the top of the simulated atmosphere are presented in Table 1 for the two cases. The total escaping flux in terms of H_2 molecules when the PRM process is included is 4.7×10^9 molecules $cm^{-2} s^{-1}$. The decrease in the atomic hydrogen population, allows for more diacetylene, in the above region, with the new simulated profile (solid line in Fig. 5c) being in good agreement with the CIRS retrieved vertical profiles (Vinatier et al., 2006).

C_6H_6: Benzene was initially detected by ISO with a mole fraction of $4 \pm 3 \times 10^{-10}$ in the stratosphere (Coustenis et al., 2003). From limb spectra, CIRS have managed to retrieve a vertical profile only for high latitudes, which represents an average between 65°N and 80°N, while for equatorial regions the derived upper limit was 1.1×10^{-9} mole fraction (Vinatier et al., 2006). From nadir spectra, a significantly improved retrieval for the abundance of this species was possible; Coustenis et al. (2007) suggested a mole fraction of $4.3^{+3.0}_{-2.5} \times 10^{-10}$ at 120 km for 33°N, while a strong latitudinal variation was observed with more than an order of magnitude increase in the stratospheric abundance when moving from 70°S to 70°N. In the upper atmosphere, the INMS detected abundance at 1200 km was of ppm order of magnitude (Waite et al., 2005), which is significantly larger than the model-derived abundances at that level.

Table 1
Mole fractions at 1200 km and escaping H and H_2 fluxes (molecules $cm^{-2} s^{-1}$) at the top of the simulated atmosphere

	Mole fraction at 1200 km		Escaping flux	
	w/o PRM	With PRM	w/o PRM	With PRM
H	5.2×10^{-4}	4.9×10^{-4}	1.0×10^9	9.3×10^8
H_2	2.9×10^{-3}	3.3×10^{-3}	3.7×10^9	4.2×10^9

The pathways of benzene formation at low temperatures are far from being well defined due to the fact that the suggested processes correspond to laboratory and theoretical work at high temperatures, as discussed also in Part I. The main production process for benzene in the upper atmosphere under the scheme used is the recombination of two propargyl radicals (C_3H_3). The high-pressure limit for this reaction has been measured (Morter et al., 1994) but the low pressure one is not known and hence must be estimated. A common approach among photochemical modellers is the use of the low pressure limit of methyl recombination multiplied by a factor of 10. Yet, the problem is far from being resolved since the rates for the methyl recombination at the low pressure limit are also not well established, as discussed previously for the case of ethane. Hence, the use of different rates can lead to mole fractions in the upper atmosphere that can vary by a few orders of magnitude. In view of the large abundances observed in the upper atmosphere, we have used the low pressure limit suggested by Moses et al. (2000) and also by Lebonnois (2005), which is significantly larger than the rate suggested by Cody et al. (2003).

The resulting vertical profile, under the scheme used in the model produces the profile presented in Fig. 5(d). The model abundance in the upper atmosphere is still significantly smaller than the INMS derived one. This probably enhances the idea that the benzene formation could be related with the ion chemistry in that region. Our vertical profile satisfies, the CIRS upper limit from limb spectra (Vinatier et al., 2006), the above described ISO disk-average observations in the stratosphere and it is well within the CIRS reported abundance at the same altitude region for mid-latitude conditions based on nadir spectra (Coustenis et al., 2007). Yet, our resulting abundance shows a different vertical variation from previous models with a minimum near 350 km. Previous photochemical models have managed to produce benzene profiles of higher abundance in the stratosphere, relative to the one reported here. Yet, these results could be over-estimated as discussed in the following paragraph. Further, the observed vertical structure from CIRS (Vinatier et al., 2006) corresponds to high latitude regions in which the enhancement due to the circulation descending cell, could enhance the mesosphere with benzene molecules produced in the upper atmosphere and remove the minimum observed in our result. In other words, we cannot exclude the possibility that the minimum observed in our profile is not present to some extent in the benzene profiles at lower latitudes. In any case, the C_6H_6 production in Titan's atmosphere still suffers from large uncertainties and the possibility of other photochemical/ion-chemistry pathways, which could lead to its production must be investigated.

C_6H_4 and C_6H_2: Also presented in Fig. 5d, are the vertical profiles of benzyne and triacetylene, respectively. The former is a direct product of benzene photolysis. Previous models have not included its photolysis. Yet based on our calculations, if it is not photodissociated, larger abundances of this species would occur in the atmosphere that would have been observed. In addition, the abundances of other species related to the C_6H_x formation are underestimated since they are effectively lost to C_6H_4. Similarly, benzyne is not efficiently lost to its precursors resulting in an increased benzene abundance, which although closer to the observed abundance it is artificial. Hence, we have decided to estimate the benzyne photolysis; Münzel and Schweig (1988) reported that electronically, C_6H_4 is similar to benzene with an additional σ bond. Hence, we have estimated benzyne photolysis with the absorption cross section of benzene and a similar photochemical scheme. With this description, a significant photolysis product of C_6H_4 is triacetylene, which explains the larger abundance obtained by our calculations for this species relative to previous photochemical models (Wilson and Atreya, 2003, 2004).

2.2.2. Nitriles

HCN and CH_2NH: The HCN vertical profile has been retrieved by ground-based millimeter (Tanguy et al., 1990; Hidayat et al., 1997; Marten et al., 2002) and submillimeter (Gurwell, 2004) observations, while the stratospheric abundances have been inferred by the Voyager IRIS disk-resolved measurements (Coustenis and Bézard, 1995), which showed the latitudinal variability due to seasonal effects, and by the ISO disk-average observations (Coustenis et al., 2003). The Cassini CIRS results have shown again that HCN has a strong latitudinal variation (Teanby et al., 2006), with stratospheric abundances increasing towards the north pole, which is entering the winter season at this time. The vertical profiles inferred at different latitudes from CIRS (Vinatier et al., 2006; Coustenis et al., 2007), depict this variation of the HCN abundance but also show that the vertical variation of the mole fraction is not with a steady slope but similar to the Marten et al. (2002) measurements, although not as steep.

The production of hydrogen cyanide is directly related to the production of atomic nitrogen from the photolysis of N_2. The latter is rapidly transformed to H_2CN and CH_2NH, which eventually provide HCN on reaction with H and photolysis, respectively. As discussed in Part I, previous photochemical models have not included or followed the production of CH_2NH in their schemes, since there is a lack of information about its photochemical properties. The main problem is the absence of reaction rates and pathways regarding the loss of methyleneimine to other species. The main production and loss mechanisms included in the model calculations are presented in Table 2.

In our calculations CH_2NH is mainly produced by:

$$N(^2D) + CH_4 \rightarrow CH_2NH + H,$$

$$NH + CH_3 \rightarrow CH_2NH + H.$$
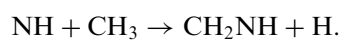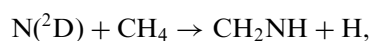
The rate for the first reaction is taken from Herron (1999) where a yield of 80% was suggested for this pathway with

Table 2
Production and loss processes for methyleneimine used in the model calculations

Reaction	Rate	Reference	T(K)
Production			
$N(^2D) + CH_4 \rightarrow CH_2NH + H$	$3.84 \times 10^{-11} e^{-750/T}$	Herron (1999)	232–292
$NH + CH_3 \rightarrow CH_2NH + H$	1.0×10^{-11}	Redondo et al. (2006)	Est.
$2\, H_2CN \rightarrow CH_2NH + HCN$	5.13×10^{-12}	Horne and Norrish (1970); Nizamov and Dagdigian (2003)	296
$CH + NH_3 \rightarrow CH_2NH + H$	$4.1 \times 10^{-9} T^{-0.56} e^{-28/T}$	Bocherel et al. (1996)	23–295
$CH_3NH_2 + h\nu \rightarrow CH_2NH + 2\, H$		See Table 3 in Part I	
Loss			
$CH_2NH + H \rightarrow H_2CN + H_2$	4.0×10^{-14}	Est. as k($CH_2O + H$)	
$CH_2NH + C_2H \rightarrow Products + H$	1.4×10^{-10}	Est. as k($C_2H_4 + C_2H$)	
$CH_2NH + CN \rightarrow H_2CN + HCN$	$6.71 \times 10^{-11} e^{-412/T}$	Est. as k($CH_2O + CN$)	
$CH_2NH + N(^2D) \rightarrow Products$	$2.3 \times 10^{-10} e^{-503/T}$	Est. as k($C_2H_4 + N(^2D)$)	
$CH_2NH + N \rightarrow H_2CN + H$	$3.32 \times 10^{-14} e^{-352/T}$	Est. as k($C_2H_4 + N$)	
$CH_2NH + H_2CN \rightarrow polymer$	$1.1 \times 10^{-12} e^{-900/T}$	Est. as k($C_2H_3 + HCN$)	
$CH_2NH + h\nu \rightarrow HCN + 2\, H$		See Table 3 in Part I	

the remaining 20% attributed to the $NH + CH_3$ pathway. Recent results by Balucani and Casavecchia (2006) at low temperatures appropriate for Titan, also suggest that the production of CH_2NH in the above reaction is the main process, possibly with a larger yield. For the second reaction, which was recently suggested to provide methyleneimine (Redondo et al., 2006), we have estimated the rate ($10^{-11}\,cm^3\,s^{-1}$) based on a comparison with other radical-radical reactions. The same approach was followed by Lellouch et al. (1994) for this reaction. For the photolysis products we have assumed a single pathway leading to HCN formation directly:

$$CH_2NH + h\nu \rightarrow HCN + 2\, H$$
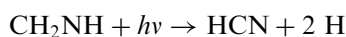
based on the results of Nguyen et al. (1996). Assuming as a photolysis product the H_2CN radical, there were no significant changes in the HCN profile, since the former readily provides the latter in reaction with H.

According to the present literature, only recently there has been some investigation of methyleneimine's UV spectrum by Teslja et al. (2004) who measured the absorption cross section in the 235–260 nm region and found it to range between 2 and $4 \times 10^{-19}\,cm^2$. We have not found any published measurements of the CH_2NH absorption cross section in any other part of the spectrum. The possible chemical loss mechanisms for CH_2NH remain another open question. Basiuk (2001) has investigated theoretically the reactions of methyleneimine with CN and HCN, water and OH. Between CN and HCN he found that although reaction with HCN is not allowed to occur, due to the presence of three high energy transition states, reaction with CN is without a barrier and can proceed readily in the gas phase. In addition, CH_2NH is isoelectronic with formaldehyde (CH_2O) and ethylene for which rates for reaction with some of the important radicals present in Titan's atmosphere have been measured. Hence, we have included reactions of methyleneimine with H,

C_2H, N, $N(^2D)$ and CN and estimated their products based on the equivalent reactions with the above two species. Finally, another possible loss mechanism could be related to the polymerization of methyleneimine, a process which is known to proceed readily for CH_2O. We have not found any published laboratory or theoretical investigation, regarding the process which could lead to the production of this polymer under the conditions found in Titan's atmosphere. Hence, we have assumed that it is initiated by the addition of H_2CN radicals similar to the process assumed from the HCN polymerization:

$$H_2CN + CH_2NH \rightarrow polymer.$$

The resulting profiles of CH_2NH and HCN are presented in Fig. 7. In order to have a view of the impact of the different processes in the final profiles, we present the calculated vertical profiles at different steps. For the methyleneimine the solid curve corresponds to the case were all production reactions presented in Table 2 are included and for the photochemical loss, there is only photolysis (case A). In case B (dashed line) the rest of the chemical reactions suggested are included. The large decrease in the profile observed above 400 km is due to the reaction with atomic hydrogen, which is the most important among those included. The N_2 dissociative ionization has also a significant impact in the upper atmosphere abundance of methyleneimine. In the previous two cases the N_2 dissociative photoinization was assumed to provide excited state N atoms. In case C (dotted line), the production of ground state N atoms is assumed. Due to the smaller abundance of $N(^2D)$ atoms in this case, the production is significantly decreased, leading to a vertical profile which is two times smaller than that of case B at 1100 km.

Yet in all cases the calculated abundance is larger than the one retrieved by the INMS measurements (Vuitton et al., 2006b) suggesting that the loss processes for CH_2NH

in the model calculations are underestimated. In view of the narrow region of the spectrum for which we have information about the absorption cross section, it is realistic to expect that there has to be some contribution to the photodissociation by the rest of the spectrum. On the other hand, reactions with other hydrocarbons and nitriles could also contribute to reducing the abundance in the upper atmosphere closer to the observed one. It is important to note that for most of the reactions assumed here, the ones that have an important role, produce either HCN directly or H_2CN that eventually yields HCN. This means that the inclusion of methyleneimine under the current scheme cannot have any important effect on the HCN profile. This is shown in Fig. 7b with the solid and
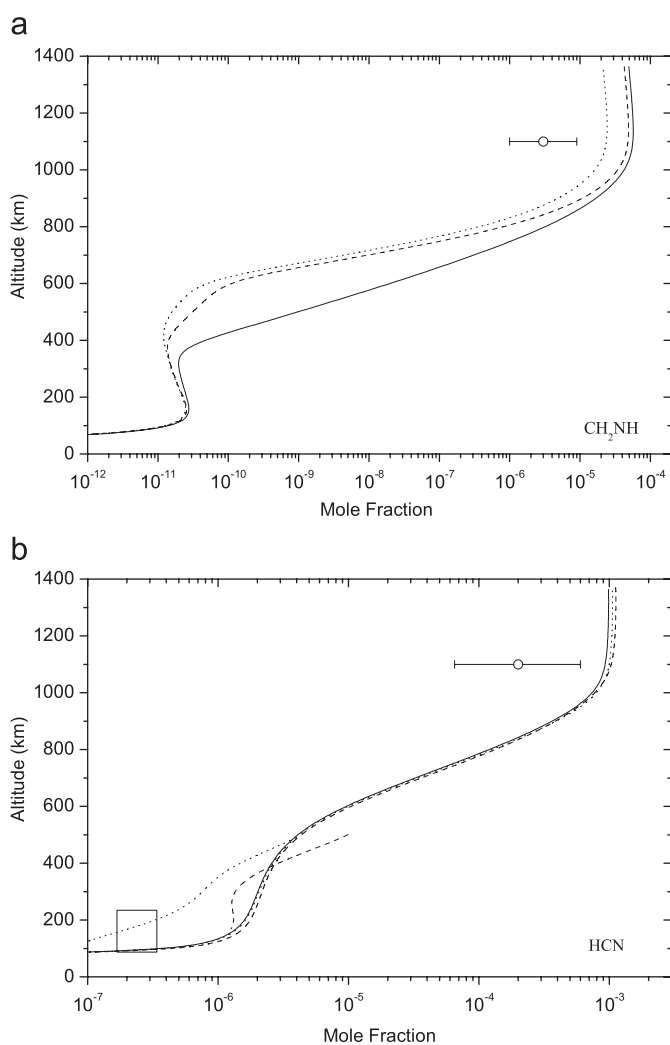

Fig. 7. Model calculated vertical profiles for methyleneimine (a) and hydrogen cyanide (b). The references for the measurements are the same as those in Fig. 4. In (a) for the solid line only photolysis is included as a loss process for CH_2NH (case A in text). For the dashed line all chemical loss processes considered are included (case B) and for the dotted line the N_2 dissociative ionization is set to yield ground state nitrogen atoms. In (b) the solid line corresponds to case B discussed above, the dashed line corresponds to the case were the evolution of CH_2NH is not followed and the dotted line presents the sensitivity of the profile on the N_2 dissociative ionization scheme.
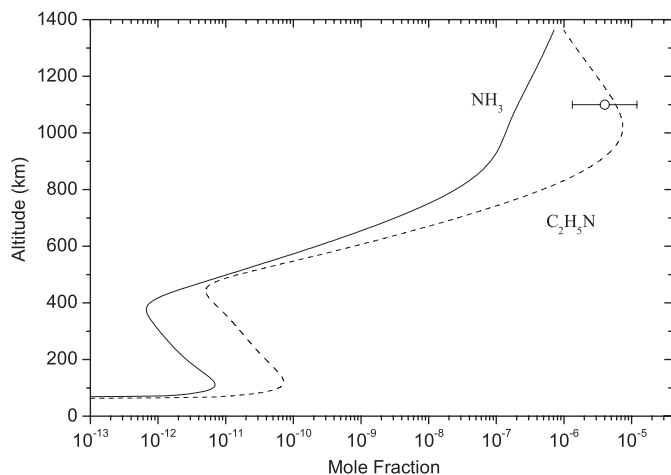
dashed lines. The latter corresponds to the case assumed in previous models where the CH_2NH was produced but its evolution was not followed. This effectively corresponds to its removal from the system. The former, represents case B discussed above, where the evolution of methyleneimine is followed. It is obvious that there are no significant changes in the HCN profile, since processes which could transform methyleneimine to other channels than HCN are of low efficiency.

As discussed previously, in the retrieval of the eddy mixing coefficient, previous works have reported the difficulty of simulating the HCN and C_2H_x stratospheric abundances with a unique mixing profile. Our resulting HCN profile presents the same problem with the mole fraction being significantly bigger than the observed abundances by CIRS measurements in the lower atmosphere. Compared to the mid-latitude stratospheric abundance retrieved by Coustenis et al. (2007) our profile is 3.3 times larger at 120 km (where the contribution function peaks), while compared to the CIRS observations at 15°S and 80°N, retrieved by Vinatier et al. (2006) (although the polar profile is affected by circulation effects) our profile is larger by 5 and 1.2 times, respectively, at 200 km.

In the upper atmosphere, the calculated mole fraction is well above the retrieved abundance by INMS (Vuitton et al., 2006a), a characteristic common in all previous photochemical models. The inclusion of the new N_2 dissociative ionization scheme produces only a very small reduction in the abundance at 1100 km relative to that with the ground state N atoms scheme (dotted line in Fig. 7b) and the calculated mole fraction (1×10^{-3}) is well above the measured 2×10^{-4}. This over-estimated production of HCN in the upper atmosphere is probably responsible for the enhanced abundance resulting in the lower atmosphere. It is evident that there is something missing in the photochemical models with regard to the description of HCN evolution. From current knowledge and estimates performed here for the properties of CH_2NH, it seems that its role is limited. Yet in order to come to a clear conclusion, new laboratory measurements regarding the reactivity of CH_2NH are needed.

NH_3: Ammonia has only been observed in Titan's thermosphere. The INMS measurements in the upper atmosphere (Vuitton et al., 2006b) retrieved a mole fraction of 4×10^{-6} at 1100 km while the model calculated mole fraction at the same altitude is about 2.1×10^{-7} (Fig. 8). Although this result is about 10 times larger than previous estimates from photochemical models (Wilson and Atreya, 2004), there is another issue. The calculated vertical profile of ethylenimine, the photolysis of which is the main source of the enhanced NH_3 production, shows a significant abundance in the upper atmosphere that has not been observed by any INMS measurements. Although we have not found any published measurements for the UV absorption cross section of C_2H_5N, and have estimated it from that of $C_2H_5NH_2$, we believe that the over prediction of the abundance of the former by the model, is not due to

Fig. 8. Calculated vertical profiles of NH_3 and C_2H_5N from the model. The open circle corresponds to the ammonia abundance retrieved by the INMS instrument (Vuitton et al., 2006b).

the possible underestimation of its cross section, but to the overestimation of its production from the reaction between $N(^2D)$ and ethane. We have assumed that the only product of this reaction to be ethylenimine, in order to investigate the maximum contribution to ammonia production. This is probably not the case with other products being more stable. From the above, we conclude that ethylenimine's production in Titan's atmosphere is smaller than that provided by the simulation, hence its role in the production of ammonia should be of secondary importance relative to the processes which allow its abundance to be closer to the observed.

CH_3CN: Acetonitrile was initially detected on Titan by Bézard et al. (1993) through heterodyne ground-based observations. Its production is dominated by the reaction of $N(^2D)$ with C_2H_4, while its loss is controlled by photolysis. This description is based on the latest measurements by Sato et al. (1999), Balucani et al. (2000a) and Payne et al. (1996), as was described by Wilson and Atreya (2004). For this species, the effects of the N_2 dissociative-ionization possible products have the most pronounced effect due to its dependence on the $N(^2D)$ population. In the model results shown in Fig. 9a, the two vertical profiles correspond to N (solid line) and $N(^2D)$ (dotted line) production by N_2 dissociative photoionization. When the nitrogen atoms are assumed to be in their ground state, the resulting acetonitrile mole fraction is about 2.4 times smaller than the one when the atoms are produced in their excited state, at 1010 km, where the maximum is observed. Assuming the production of ground state nitrogen atoms, a vertical profile is produced that is closer to the observations. Although for both cases the upper atmosphere abundance calculated by the model is overestimated relative to the INMS derived mole fraction (Vuitton et al., 2006b), the agreement is significantly improved in the lower atmosphere relative to the Marten et al. (2002) retrieved abundance at 400 km for the case of

$N(^4S)$ production. The model profile suggests a larger abundance of acetonitrile in the region below, compared to the observations. It is important to note that the above disk-average observations, as the authors report, are representative of low latitude regions. This could explain the different slope observed between the measurements and model in the region between 150 and 400 km since our calculations are representative of mid-latitude regions, which are expected to have an enhanced nitrile abundance.

C_2H_3CN: The production of acrylonitrile in the upper atmosphere is controlled by the reaction of CN radicals with ethylene. Although the rate for this reaction has been measured down to very low temperatures (Sims et al., 1993), the possible products have been a subject of debate for some time. Monks et al. (1993) measurements suggested a yield of 20% for acrylonitrile with the rest 80% attributed to the C_2H_3 + HCN formation. This branching ratio is used in most of the published photochemical models of Titan's atmosphere. More recently, Balucani et al. (2000b) have reported the production of C_2H_3CN but were unable to detect HCN and C_2H_3 due to the high background signal at $m/e = 27$ in their experiment. The RRKM theoretical investigation by Vereecken et al. (2003) suggested that the major product is acrylonitrile with the HCN pathway becoming important only at high temperatures ($T > 1000$ K). Recently Choi et al. (2004) suggested a branching ratio of 1 for acrylonitrile production, by measuring the H atom branching ratio at room temperature. The recent results from INMS for the composition of the upper atmosphere (Vuitton et al., 2006a), also show that the mole fraction of acrylonitrile is about an order of magnitude higher than those suggested by previous photochemical models, assuming the Monks et al. (1993) branching ratio. Based on the above, in the current calculations we have attributed the products of the CN + C_2H_4 reaction solely to acrylonitrile production. The model calculated profile (Fig. 9b) is in very good agreement with the observed abundance in the upper atmosphere.

Until now there has been no observation of C_2H_3CN in Titan's lower atmosphere. There, its production depends on the reaction of hydrogen cyanide with vinyl radical (C_2H_3). The rate of this reaction has also been measured by Monks et al. (1993) at room temperature, with the reported temperature dependence assumed based on similar reactions of C_2H_3 with acetylene and ethylene. The reaction was suggested to lead to the formation of acrylonitrile based on thermochemical considerations, although C_2H_3CN was detected only in trace amounts. Previous photochemical models concluded that the inclusion of this pathway with the suggested rate, leads to excessive production of acrylonitrile in the lower atmosphere, well above the detection limit placed by ground-based observations ($\sim 2 \times 10^{-9}$, Marten et al., 2002) with mole fraction values reaching above 10^{-8} in Wilson and Atreya (2004). Our results provide a stratospheric abundance for C_2H_3CN that is just above the upper defined limit. This improved agreement, is mainly related to chemical loss to haze, which
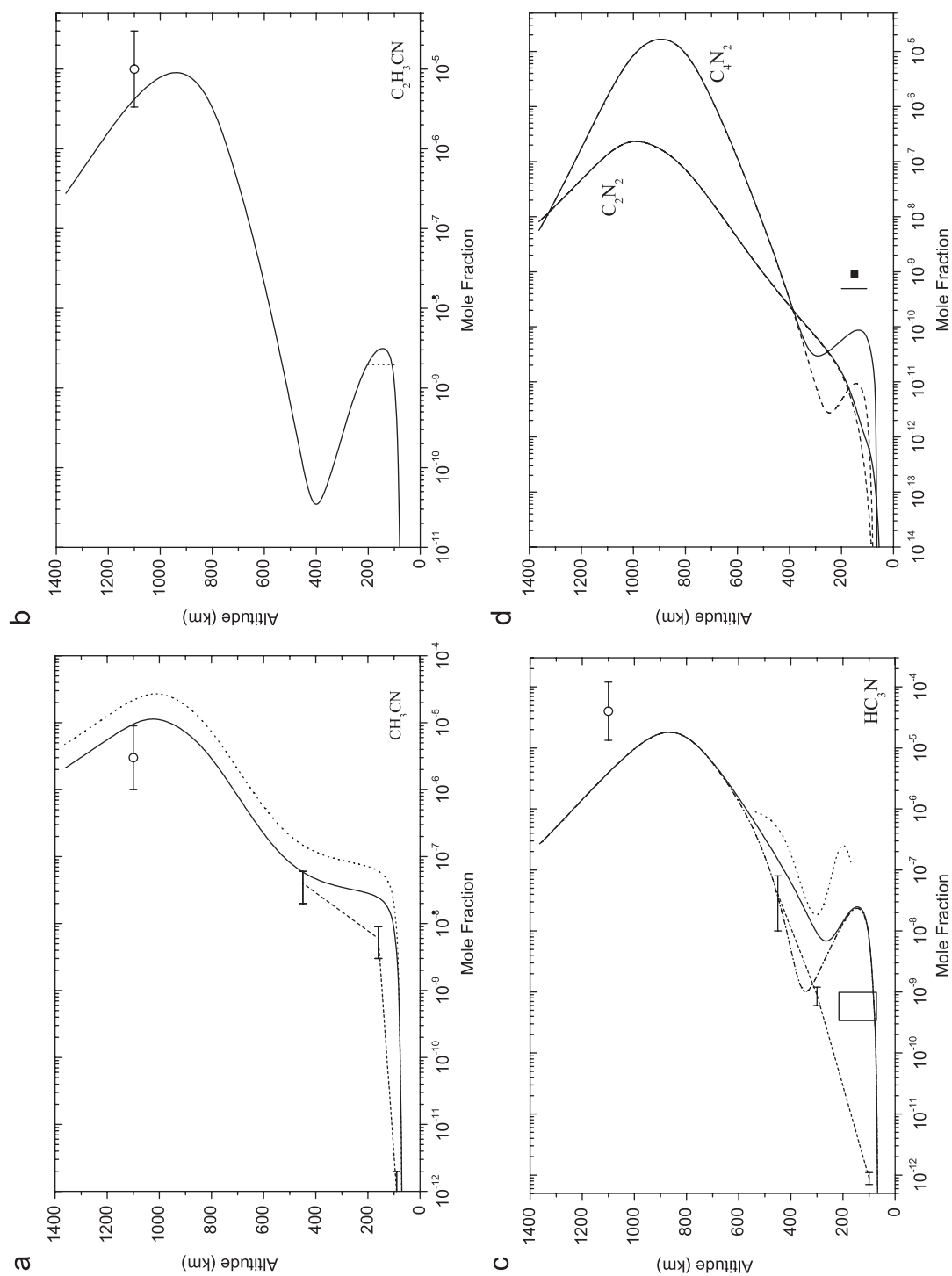
Fig. 9. Model vertical profiles for the main nitrile species observed in Titan's atmosphere. Open circles correspond to the INMS derived abundances from Vuitton et al. (2006a, b), horizontal error bars connected with dashed lines present the Marten et al. (2002) ground-based observations and the box represents the CIRS observations from Coustenis et al. (2007). The vertical line and the filled square correspond to the upper limit-low latitude and high northern latitude retrieved abundance, respectively, for C_2N_2 from CIRS measurements by Teanby et al. (2006). In (a) the solid and dotted lines present the sensitivity of the profile on the N_2 dissociative ionization scheme. In (c) the solid and dash-dotted lines correspond to the model results with and without the PRM process, respectively. In (d) solid and dashed lines correspond to the inclusion or not of the GCR impact, respectively.

is specifically described in the current work (see next section). In addition, the larger mixing profile in the lower atmosphere, constrains the mole fractions of species in this region to smaller values, since it increases their flow towards the condensation region where they are irreversibly lost.

HC_3N: The photolysis of the produced acrylonitrile is the main source for the formation of cyanoacetylene. This is enhanced in the upper atmosphere by the reaction of CN radicals with acetylene, while the main loss mechanisms are photolysis and reaction with atomic hydrogen:

$$H + HC_3N + M \rightarrow H_2C_3N + M.$$
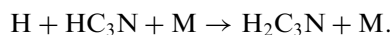
The high pressure limit of the latter has been recently measured for the first time by Parker et al. (2004) down to 200 K and was found to be about 4 times faster at this temperature, than that of the equivalent reaction with acetylene:

$$H + C_2H_2 + M \rightarrow C_2H_3 + M$$

which was used in previous models for the estimation of this rate. In addition, based on their measurements at different pressures, the authors concluded that the pressure dependence for this reaction is smaller than that of the equivalent reaction with C_2H_2, which means that the reaction proceeds with a significant rate even at small pressures.

The model vertical profile of cyanoacetylene is presented in Fig. 9c. Although our calculated profile for acrylonitrile is in good agreement with the INMS derived abundance in the thermosphere (Vuitton et al., 2006a), the model cyanoacetylene in the upper atmosphere is below the retrieved abundance. The contribution of the acetylene based pathway:

$$CN + C_2H_2 \rightarrow HC_3N + H$$
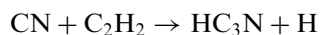
has a comparable magnitude at these altitudes with that of C_2H_3CN photolysis. But, in view of the reasonably good agreement of the model with the C_2H_2 profile, we cannot expect a significant enhancement of the model acrylonitrile by improving the match to this species either. This probably suggests that other processes not included in the model enhance the production of HC_3N in the upper atmosphere.

In the stratosphere it is important to note the effects of the heterogeneous process described previously on the model HC_3N vertical profile. When the heterogeneous hydrogen scavenging is not included, the large atomic hydrogen population that is allowed to survive in the mesosphere, leads to a large chemical loss through the formation of H_2C_3N discussed above. This loss brings the calculated mesospheric mole fraction (dashed-dotted line in Fig. 9c) below the retrieved mole fraction from the ground-based observations in the region between 350 and 450 km (Marten et al., 2002). When the atomic hydrogen population is strongly reduced by the inclusion of the heterogeneous process (solid line in Fig. 9c), the HC_3N

profile increases towards the polar profile retrieved by the CIRS observations (Vinatier et al., 2006).

Yet in both cases the calculated mole fractions below 350 km increase due to the contribution of the photolyzed C_2H_3CN in this region. This brings the model abundance in the stratosphere closer to the mole fractions reported by CIRS for higher latitudes compared to the mid-latitude reported abundance (Coustenis et al., 2007), shown in Fig. 9c. It is important to note that the model abundance for C_2H_3CN, which has not been detected in Titan's stratosphere, is very close to the upper detection limit defined by the observations. Hence, the possibility of an enhanced production for this species by the model calculations compared to that actually present (but not detectable) in Titan's stratosphere, leading eventually to an increased HC_3N abundance in this region, cannot be excluded.

C_2N_2 and C_4N_2: Cyanogen and dicyanogen are presented in Fig. 9(d). CIRS observations (Teanby et al., 2006) have managed to retrieve an upper limit of 5×10^{-10} for the low latitude regions increasing to a mole fraction of $\sim 9 \times 10^{-10}$ at 50°N, both at 3 mbar ($\sim$150 km). No information for gaseous C_4N_2 has been published so far. Our calculated profile for C_2N_2 is well below the previous upper limit, with a mole fraction of 3.9×10^{-12} at 150 km. As reported by previous works also, the vertical profiles of these two species demonstrate the significant impact of the GCR process with an increase observed when the enhanced N_2 destruction is included. This is presented with the dashed lines in Fig. 9d, which correspond to the model calculated profiles if the galactic cosmic rays are not included. Yet the contribution of GCR, based on our results is significantly smaller than the one reported by Wilson and Atreya (2004). The latter, reported an increase of the C_2N_2 abundance in the stratosphere larger than 6 orders of magnitude with the mole fraction reaching very close to the reported upper limit from CIRS. The reasons for this disagreement between the two model results is not clear to us.

In Table 3 the model calculated photochemical column production and loss rates along with the net production for the major species in Titan's atmosphere are presented. For N_2 and CH_4, which are the only species (along with argon) for which we kept their surface abundance fixed, assuming there is a constant supply from the surface, the net production is negative demonstrating the fact that these species are destroyed and so provide the rest of the chemical composition that is observed. For all other long-lived species the net production is positive, since these are present in the atmosphere after the convergence to a steady state. Their vertical profiles are determined by a balance between diffusion, loss due to escape to space and/or condensation and surface deposition. Note that reactions leading to unknown species (products in reactions tables) along with those for the haze pathways, act as a sink for the atmospheric C, N and H atoms. When these losses are taken into account the photochemical production and loss are balanced.

Table 3
Column photochemical production and loss rates for the main hydrocarbon and nitrile species in Titan's atmosphere in $cm^{-2}\,s^{-1}$

Species	Production	Loss	Net production
H	1.6×10^{10}	1.2×10^{10}	3.8×10^9
H_2	8.5×10^9	3.0×10^9	8.2×10^9
CH_4	7.5×10^8	1.4×10^{10}	-1.3×10^{10}
C_2H_6	4.7×10^9	6.0×10^8	4.1×10^9
C_2H_4	1.9×10^9	1.8×10^9	6.0×10^7
C_2H_2	1.2×10^{10}	1.1×10^{10}	3.2×10^8
CH_3C_2H	9.7×10^7	9.5×10^7	2.3×10^6
C_3H_8	4.8×10^8	1.1×10^8	3.7×10^8
C_4H_2	2.6×10^9	2.6×10^9	4.6×10^6
C_6H_6	3.8×10^8	3.8×10^8	2.1×10^5
N_2	1.1×10^8	4.7×10^8	-3.6×10^8
HCN	2.3×10^9	1.9×10^9	3.2×10^8
CH_2NH	5.3×10^7	5.3×10^7	3.7×10^4
NH_3	2.7×10^6	2.6×10^6	6.7×10^4
CH_3CN	2.7×10^7	1.0×10^7	1.7×10^7
C_2H_3CN	1.6×10^9	1.6×10^9	2.8×10^5
HC_3N	1.2×10^9	1.1×10^9	9.2×10^6
C_2N_2	3.5×10^5	3.3×10^5	2.6×10^4
C_4N_2	1.1×10^8	1.1×10^8	1.9×10^6

When all species are included along with losses to unknown species (products in reactions tables) and to haze formation, the C, N and H atoms are in photochemical balance. Rates are referred to the surface.

From the above results we conclude that the model successfully reproduces the observed abundances for the upper atmosphere, retrieved by INMS for most of the hydrocarbons. C_2H_6, C_2H_4, C_2H_2 and C_3H_4 are well reproduced, while C_4H_2 is just below the observed lower limit, and only C_3H_8 and C_6H_6 are significantly underestimated. For the nitrile species, the model results are again close to observed abundances but the agreement is not as good as that observed for the hydrocarbons. The resulting HCN abundance is above the observed upper limit, which is also the case for CH_3CN and CH_2NH, while the case reverses for HC_3N and NH_3 for which our calculated abundances are below the lower defined limit. The calculated abundance for C_2H_3CN provides an excellent fit to the observed one. In the region of the INMS observations (thermosphere) the atmosphere is expected to be well mixed, thus dynamical effects are not expected to have a significant impact on the observed abundances. This means that the observed difference should be attributed to the photochemical description (rates and yields used). Further, the large number of new nitrile species observed by INMS in the upper atmosphere (Vuitton et al., 2006b), which are not included in the current calculations, could possibly have an impact on the above species, leading to the observed abundances.

In the region of the CIRS observations (stratosphere) dynamical processes are expected to have a stronger effect. This is more well observed for the case of C_2H_4 as discussed above. The model results for C_2H_6, C_4H_2 and

C_6H_6 are in close agreement with the observed abundances, while C_2H_2 is slightly below the observed profiles below 300 km. For CH_3C_2H and C_3H_8 the model underestimates and over-estimates their abundances, respectively. A possible reason for this discrepancy is presented in the last section, regarding the role of the methyl radicals. For nitriles, the simulated HCN is above the observed range of abundances. For the rest of the observed nitriles in this region (CH_3CN, HC_3N, C_2H_3CN), the model is in agreement with the abundances and upper limits set by CIRS and ground-based observations.

3. Haze pathways

In the previous section the results of our model calculations regarding the vertical chemical composition of Titan's atmosphere were described. The overall picture is in good agreement with the retrieved abundances from the latest measurements taken by the instruments of the Cassini/Huygens mission. This suggests that the model generated haze opacities, based on the suggested pathways described in Part I, which affect the solar radiation fluxes responsible for the photolysis of the species and the vertical temperature profile, provide an adequate equivalent of the ones found in Titan's atmosphere. In this section, a description of the contribution of each pathway is presented.

3.1. Aromatics

In the aromatics family we have included both pure hydrocarbon and copolymer structures (see Fig. 10a). The polymer structures initiated with the acetylene addition on phenyl radicals provide the major contribution for this family with a peak at 140 km and a rate of 2.3×10^{-2} particles $cm^{-3}\,s^{-1}$. As discussed in Part I also, we have used the pressure-dependent rate of Wang and Frenklach (1994) for this reaction, since the stabilized adduct is the one that leads to the formation of PAH structures. When this rate is compared with the high-pressure limit rate for the adduct formation reported by Yu et al. (1994) and not with the total reaction rate, which is pressure independent, it becomes apparent that the two rates, in the temperature range between 100 and 200 K, characteristic for Titan's conditions, are in much better agreement.

The aromatic copolymer structures based on the cyanoacetylene addition on phenyl radicals have a smaller contribution than the PAH formation pathway. It peaks at 135 km with a production rate of 3.7×10^{-4} particles $cm^{-3}\,s^{-1}$. We have estimated the rate for this reaction with the pressure-dependent rate for the acetylene addition. Both the above two aromatic pathways, decrease with altitude due to their pressure dependence. The third aromatic pathway used, that of direct phenyl addition on benzene molecules has a very small contribution, due to the low abundances for both of the reacting species.
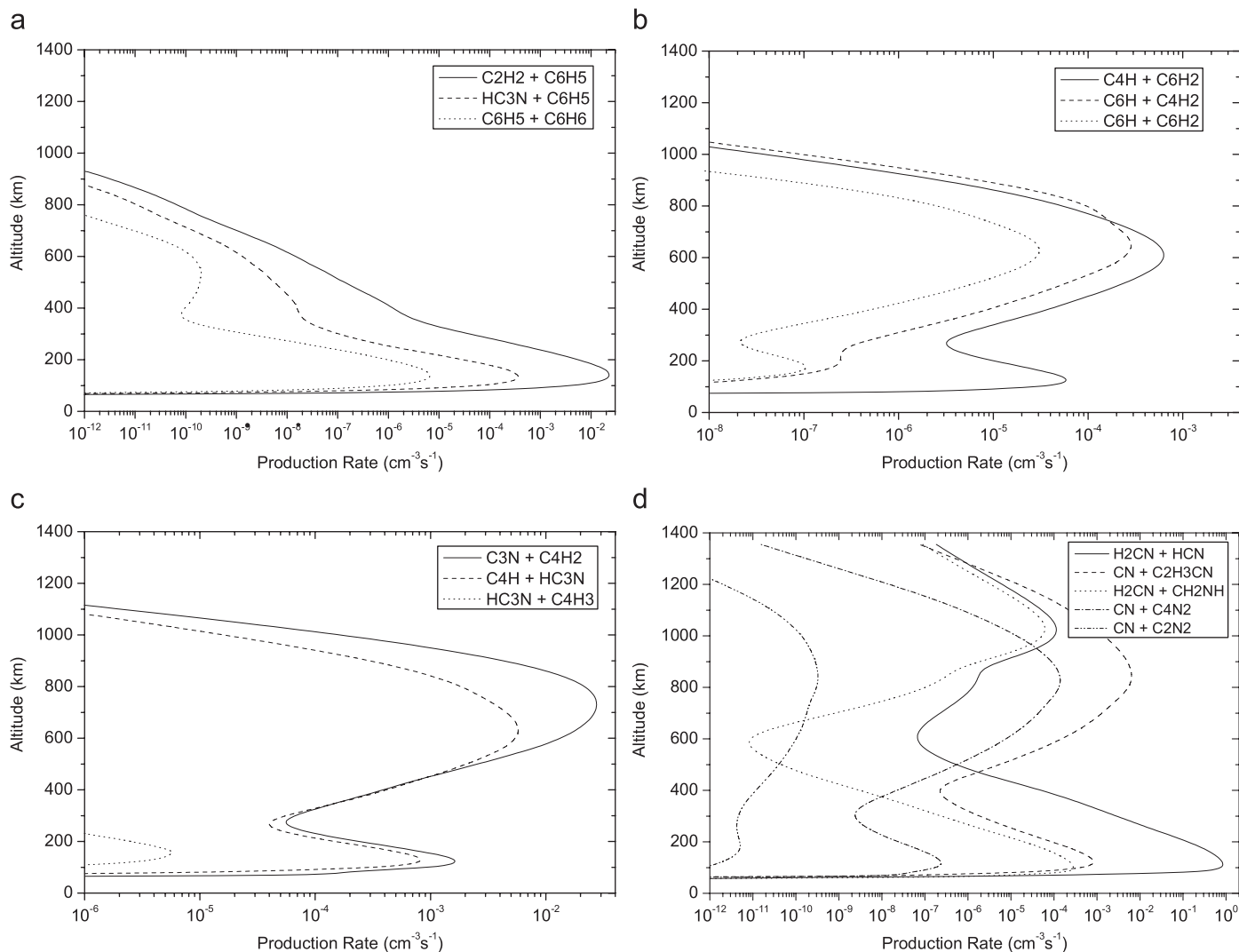
Fig. 10. Vertical haze production profiles from the contribution of each reaction in the main families discussed in the text: (a) Aromatics; (b) Polyynes; (c) Pure nitriles; (d) Copolymers.

Although benzene formation, as discussed in the previous section, still suffers from large uncertainties in the upper atmosphere, the role of aromatic chemistry in haze formation based on these pathways is a first step towards an estimation of their contribution. Since, based on our calculations and those of others, their contribution is important only in the lower atmosphere, where the model resulting benzene profile is within the range of latitudinal values reported by CIRS, we have included them in the total haze production rate.

3.2. Polyynes

Polyyne formation is based on C_4H_2 and C_6H_2 species in our description and proceeds with the addition of C_4H and C_6H radicals (Fig. 10b). The main peak of the total polyyne contribution is situated at 620 km with a production rate of 9.2×10^{-4} particles $cm^{-3} s^{-1}$, which is very small compared to the total column production from all the pathways (Fig. 11). This is something which is expected, as discussed
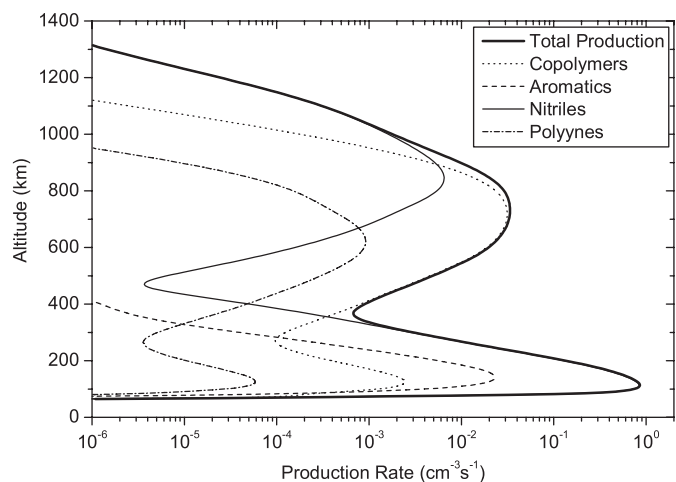

Fig. 11. The vertical production profile of haze particles (monomers) according to the model calculations and based on the calculated chemical composition. Each one of the thin lines corresponds to the contribution of a different family of polymer structures, while the thick line corresponds to the total production rate.

in Part I, due to the decreasing abundance of polyynes with increasing size of these molecules. Compared to the production profile of polyynes reported in Wilson and Atreya (2003), our monomer production profile is larger due to the increased abundance of C_4H_2 in our calculations compared to their profile. On the other hand, our calculated profile is very close to the lower boundary of the retrieved abundance by INMS, which means that possibly the contribution of polyynes is slightly larger in the upper atmosphere, than the one suggested by our calculations. Yet, the total production in this region is dominated by the aliphatic copolymer contribution, which means that even if our polyyne production is slightly underestimated, this will not be significant for the total haze production profile.

3.3. Aliphatic copolymers

Aliphatic copolymers are based on the Clarke and Ferris (1997) suggestion for HC_3N/C_2H_2 copolymers. Based on the pathways we use, their contribution dominates the total production rate above 300 km with a peak at ~720 km of 3.1×10^{-2} particles $cm^{-3}s^{-1}$. The two different pathways included

$$C_3N + C_4H_2 \rightarrow polymer$$

$$C_4H + HC_3N \rightarrow polymer$$
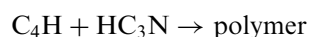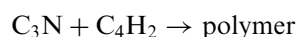
have comparable contributions, with the first being slightly larger in the upper atmosphere (Fig. 10c). The third pathway for this family, based on the

$$HC_3N + C_4H_3 \rightarrow polymer$$
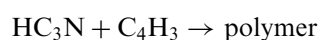
pathway (Lebonnois et al., 2002), has a significantly smaller contribution due to the pressure dependence of the rate.

Our aliphatic copolymer pathways have a main contribution in the upper atmosphere, which was not present in previous model results. The high altitude production of particles generated by this family is very important in the model calculations. This is because it provides a significant source of opacity in the upper atmosphere which is necessary in order to match the observed haze extinction profiles (Tomasko et al., 2005) and as a consequence, the observed vertical temperature structure. These are discussed in more detail in the next section.

3.4. Pure nitriles

As discussed in Part I, the nitrile species involved in the pathways of haze formation are HCN, H_2CN, CH_2NH, C_2H_3CN, C_2N_2 and C_4N_2. In the upper atmosphere the nitrile contribution is dominated by the reaction

$$CN + C_2H_3CN \rightarrow polymer$$

due to the large observed abundance of C_2H_3CN in this region, while in the lower atmosphere, the largest

contribution comes from the

$$H_2CN + HCN \rightarrow polymer$$

pathway (see Fig. 10(d)). This qualitative picture is similar to the one suggested by Wilson and Atreya (2003) although the quantitative details are different due to the different vertical profiles of the precursor species calculated by the two models. Our total nitrile contribution in the upper atmosphere peaks at 845 km with a production rate of 6.5×10^{-3} particles $cm^{-3} s^{-1}$, while Wilson and Atreya (2003) suggest a peak at about the same region but with more than an order of magnitude smaller production rate. This is due to the underestimation of the C_2H_3CN abundance in the upper atmosphere, in their pre-Cassini model results. The CN addition mechanism is also important for the case of C_4N_2, with this pathway providing the second most important contribution of the pure nitrile pathways in the upper atmosphere, after the C_2H_3CN contribution, although of significantly smaller magnitude. Due to its small abundance, the C_2N_2 pathway has a negligible contribution.

On the other hand, in the lower atmosphere, their suggested contribution from the H_2CN pathway peaks at about 200 km, while our results suggest a peak significantly lower, at ~115 km. This difference is probably related to the different structure of the calculated HCN profiles in this region by the two models, with our more constant profile below 300 km, providing an enhanced contribution by this pathway below 200 km. Further the pathway based on the polymerization of CH_2NH (along with the acrylonitrile pathway) provides the second most important nitrile contribution in the lower atmosphere while its contribution becomes important again in the upper atmosphere, above 1000 km although the suggested production rate in this region could be overestimated due to the large abundance suggested by our model calculations for CH_2NH, relative to the observed one.

3.5. Haze production profile and the role of GCR

The total vertical production rate, along with the contribution of each family is presented in Fig. 11. From the above description it becomes evident that there are specific altitude regions where the contribution of each family is important. In the lower atmosphere, below 300 km, the production is controlled by the nitrile family along with the aromatics. At higher altitudes, the aliphatic copolymers dominate the production up to 1000 km, while at even higher levels, the nitrile contribution dominates again. Polyynes are found to be of secondary importance compared to all other families.

This picture of varying production and composition with altitude is a representation of the photochemical background of haze formation, under the current description. Nitriles, are produced at very high altitudes, due to their dependence on the N_2 destruction. The last is possible only by high energy UV photons, which have their maximum

deposition above 1000 km, based on our calculations. Hydrocarbon production, which is initiated by methane photolysis, has its maximum at lower altitudes due to the absorption of these species at longer wavelengths with increasing carbon complexity (CH_4 photolysis has its maximum deposition at ~800 km, see Fig. 4 in Part I). Hence, above 1000 km, nitrile pathways dominate haze production, while below the combined contribution of nitriles and hydrocarbons increases. Finally, at lower altitudes pure hydrocarbons start to have a larger contribution.

At this point it is important to note the significance of GCR impact in the haze production profile. In particular, H_2CN and CH_2NH exhibit a large variation in their stratospheric profile when galactic cosmic rays are included, with their abundances increasing significantly (Fig. 12a). This translates to a large contribution to the haze production profile in this region from the pathways that are based on them and explains why the nitrile family starts to become important again below 300 km. This effect is presented in Fig. 12b where the total vertical production rate for the haze monomers is shown with and without the GCR contribution. When it is removed, the decrease in the H_2CN and CH_2NH stratospheric abundance, practically removes the contribution of nitrile pathways in the lower atmosphere. From the above, it is clear that the temporal character of GCR could lead to temporal variations in total haze production.

Under this description, it is evident that the contribution of pure hydrocarbon pathways is only significant in the lower atmosphere, through the aromatic polymer pathway, since the contribution from polyynes is significantly smaller than that of all other families. Yet, even in the lower atmosphere, the total production, when the GCR are included, is dominated by the nitrile pathways. This small contribution of pure hydrocarbon pathways in the haze vertical production, seems to be in keeping with the measurements from the ACP instrument on board the Huygens probe (Israël et al., 2005). These measurements, as discussed also in Part I, provide evidence of nitrogen incorporation in the haze particles, based on the pyrolysis products of the sampled aerosols. Neglecting the pathways of pure hydrocarbons in haze formation does not change significantly the vertical structure of the produced haze particles, since their contribution to the vertical production profile is in the same region as that of the other pathways. The difference will be only in the total haze opacity. For the current calculations we have included the pure hydrocarbon contribution.

The column production rate from all of the above pathways is 9.0×10^6 particles $cm^{-2} s^{-1}$, which corresponds to 1.27×10^{-14} g $cm^{-2} s^{-1}$ for the 7.25 Å radius used for the monomers. This value is within the range $0.5–2\times 10^{-14}$ g $cm^{-2} s^{-1}$, reported in McKay et al. (2001) from previous photochemical and microphysical models along with laboratory simulations. Care should be taken when comparing results from different works because the size of the monomers used is usually not the same and this can lead to slightly different results regarding the column production rate. In addition, the assumed shape of the particles (spherical or fractal), is known to lead to significantly different results for the column production rates, with the fractal aggregates usually requiring larger production rates than those with spherical shape (McKay et al., 2001). Nevertheless, our column production is in good agreement with previous estimates based on spherical particle calculations. The contribution of each family to the total column production is presented in Table 4 along with
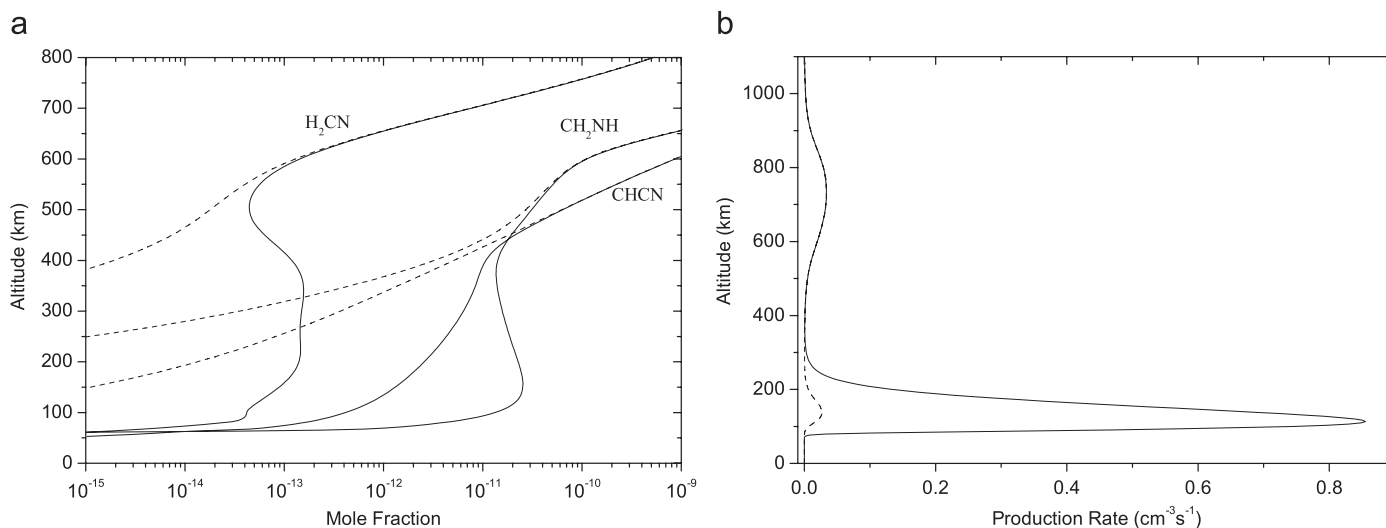

Fig. 12. (a) The impact of GCR on the vertical profiles of CHCN, CH_2NH, and H_2CN. Solid lines include the GCR contribution while dashed lines correspond to no GCR impact. (b) GCR have a broad contribution in the haze vertical production profile in the lower atmosphere. The vertical production profile shown with the solid line is the same as that in Fig. 11, but on a linear scale. The dashed profile corresponds to the resulting production profile when GCR are not included. In this case the production in the lower atmosphere is controlled by the aromatic family. The two profiles converge at higher altitudes where the impact of GCR is negligible.

the contributions in the upper (300–1500 km) and lower (0–300 km) atmosphere.

3.6. Chemical loss to haze

The total number of C, N and H atoms lost in the formation of the initial dimer and chemical growth to the size of the monomer, beyond which microphysical growth takes over, is presented in Table 4. Due to the dominance of the pure nitrile and copolymer pathways in the haze production, the total number of nitrogen atoms lost to the haze is significant. With the column atomic nitrogen production from N_2 destruction being $7.3 \times 10^8 \, cm^{-2} \, s^{-1}$ from our calculations, the loss to haze formation corresponds to ∼40% of the total N production. The importance of this nitrogen loss was initially suggested by McKay (1996) who estimated it to be about 12% of the total atomic nitrogen production in the upper atmosphere,

based on the total C and N produced in the photolysis of CH_4 and N_2 and assuming a C/N ratio of 4, taken as an average from the laboratory derived ratios. Our results, which are specifically based on the chemical loss to haze and not the total production of C and N, suggest C/N and C/H ratios which are about 1.3 and hence approximately correspond to a stoichiometric formula of $C_4H_3N_3$ for the haze particles.

The initial chemical loss for the dimer formation is of significantly smaller magnitude than the total chemical loss for the growth to the size of the monomer (see ε factors presented in Table 6 in Part I). This means that, if only the chemical loss for the formation of the dimer is included in the calculations, there will be an underestimation of the impact of haze formation in the atmospheric gas composition. This is presented in Fig. 13a, where the vertical profiles of the main hydrocarbons and nitriles are presented with and without the inclusion of the chemical loss through the chemical growth of the dimers to the monomer size. The impact of this process is more important for nitrile species than hydrocarbons. This is expected since the relative loss of carbon to haze is smaller than that of nitrogen.

Based on the possible importance of haze formation as a nitrogen sink, Lara et al. (1999), suggested that the loss of HCN through polymerization, could be a possible process for the reduction of the stratospheric HCN abundance and the correct representation of this species along with the C_2H_x carbons with the use of a single eddy mixing profile. They concluded that for the process to be efficient, a loss rate of the order $(3-5) \times 10^8 \, cm^{-2} \, s^{-1}$ was necessary, while Vinatier et al. (2006) reached a similar conclusion regarding the total loss rate of HCN needed to be used in their

Table 4
Column production rates for the families studied at different regions of the atmosphere along with the total C, N and H lost in the chemical formation and growth of the haze monomers

Family	Column production rate			Total chemical loss		
	0–300 km	300–1400 km	Total	C	N	H
Aromatics	1.9(5)	1.1(2)	1.9(4)	1.5(7)	4.4(4)	1.4(7)
Polyynes	5.0(2)	2.5(4)	2.5(4)	2.0(6)	0	5.9(5)
Nitriles	7.1(6)	2.6(5)	7.4(6)	2.8(8)	2.7(8)	2.7(8)
Copolymers	2.0(4)	1.4(6)	1.4(6)	8.8(7)	2.2(7)	7.1(6)
Total	7.4(6)	1.6(6)	9.0(6)	3.8(8)	3.0(8)	2.9(8)

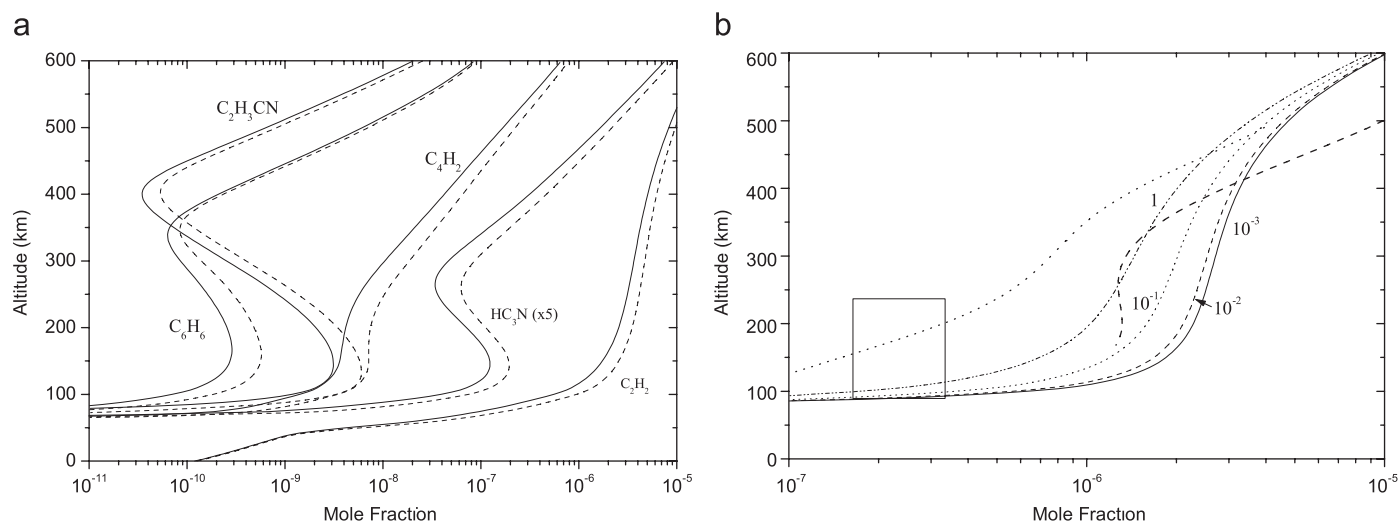Read a(b) as $a \times 10^b$. Units are in $cm^{-2} \, s^{-1}$.

a

b

Fig. 13. (a) The impact of chemical loss due to haze monomer production on the vertical profiles of species involved in the pathways. Solid and dashed lines correspond to the model results with and without the chemical growth of the initial dimers, respectively. Notice that the HC_3N vertical profiles are multiplied by a factor of 5 for clarity. (b) The impact of haze formation on the HCN vertical profile for different $H_2CN + HCN$ reaction rates. For the solid line the rate was estimated with the Monks et al. (1993) measured rate for the reaction $C_2H_3 + HCN$ rate, while dashed, dotted lines and dashed-dotted lines correspond to 10^{-1}, 10^{-2} and 10^{-3} times the Monks et al. (1993) rate. Also shown are the CIRS retrieved vertical profiles for equatorial and polar regions based on limb spectra (Vinatier et al., 2006) and the CIRS mid-latitude stratospheric abundance based on nadir spectra from (Coustenis et al., 2007).

calculations to match the CIRS retrieved vertical profiles of C_2H_6 and HCN with a single mixing profile.

According to the description provided above, the major HCN loss (and nitrogen loss at the same time) due to haze formation is from the

$$HCN + H_2CN \rightarrow polymer$$

pathway. Yet, the magnitude of the process depends on the rate used for the formation of the initial dimer and as discussed in Part I, the rate for this reaction is not measured but estimated based on the $C_2H_3 + HCN$ reaction measured by Monks et al. (1993). Wilson and Atreya (2003) have used a reduced rate for this reaction based on their results regarding the C_2H_3CN and HC_3N profile along with the total haze production generated in their calculations, while in Part I we have discussed a possible reason for the reduction of this reaction rate. Nevertheless, we have performed a sensitivity test for the effects of the rate used. Fig. 13b presents the calculated vertical HCN profile from our calculations for four different estimations of the ratio

$$\gamma = \frac{k(H_2CN + HCN)}{k(Monks\ et\ al.,\ 1993)} \tag{1}$$

ranging between one and a 1000 times smaller rate. From the presented results it is obvious that the higher the rate of the reaction, the stronger the decrease in the HCN profile observed. Setting γ to 1, provides a loss rate for the HCN molecules due to haze production that is sufficient to constrain the calculated profile within the bounds of the observations in the stratosphere. In terms of HCN molecules lost, the column rate is $4.2 \times 10^8\ cm^{-2}\ s^{-1}$. Yet, in view of the over-estimation of the HCN abundance in the upper atmosphere, which leads to larger fluxes towards the lower atmosphere and the expected reduced rate of the reaction discussed in Part I, we have kept γ to 0.1. All results presented so far are for this value of γ. The increased nitrile loss for increasing values of γ has also an impact on the resulting C/N ratio which decreases by a factor of 2.5 for γ values between 10^{-3} and 1 (Table 5).

Changing the rate for the $H_2CN + HCN$ reaction changes the total haze production. Yet, the increase in the monomer production is counter-balanced by the loss of the precursors. This is presented in Fig. 14. There the model calculated column production of particles due to this pathway is presented along with the resulting HCN mole fraction at 200 km and haze column opacity at 530 nm, for
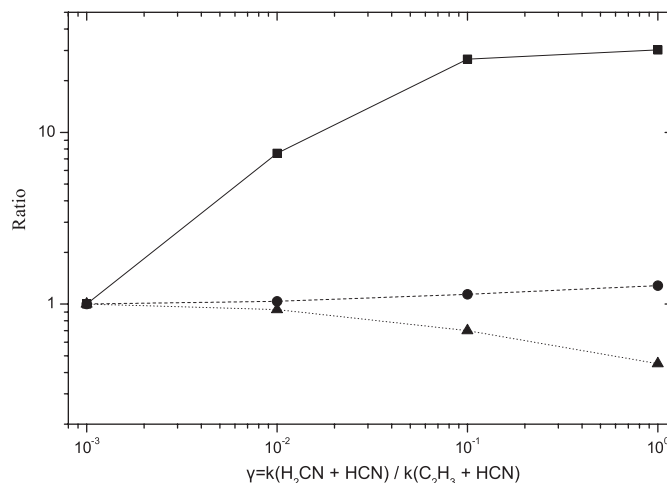

Fig. 14. Variation of column haze production through the H_2CN + HCN pathway (squares), HCN mixing ratio at 200 km (triangles) and haze opacity at 530 nm (circles) for different values of the ratio γ. All values have been normalized to unity for $\gamma = 10^{-3}$.

different values of the γ ratio. All values have been normalized to unity for $\gamma = 10^{-3}$. The chemical loss of HCN resulting from the above reaction constrains the increase in haze production. As γ increases from 10^{-3} to 1, the column production increases by a factor of $\sim$30, while the HCN mole fraction at 200 km decreases by 0.45. At the same time, because the increase in the production is located in the lower atmosphere, the change in the resulting haze opacity is minimal (for $\gamma = 1$ the ratio of the opacities is $\sim$1.3). This happens because the large downwelling fluxes present in the lower atmosphere force the particles to flow fast towards the surface where they are irreversibly lost.

The above picture would be much different without the inclusion of the chemical loss in the growth of the dimers to the monomer size. As discussed above, the chemical loss due to the dimer formation is significantly smaller than the total chemical loss due to the haze production. Hence, if the latter is not included, the increased production will not be constrained by the loss of the precursors and the total haze produced will be too large to match the observed geometric albedo. Previous results from Wilson and Atreya (2003, 2004) do not specifically mention the inclusion of this process in their calculations although their HCN vertical profiles seems to be in agreement with the observed stratospheric abundances.

4. Haze radiative properties

Using the above-described production profile for the haze particles, the microphysical part of the model provides a description for the evolution of the monomers to the observed particle size in Titan's atmosphere. The produced size distribution along with the resulting optical properties of the haze layer generated with the use of Mie theory are described in this section and are validated against the

Table 5
Variation of C/N and C/H ratios for different values of the γ ratio along with the column production rate (CPR) from all included pathways in $10^{-14}\ g\ cm^{-2}\ s^{-1}$

γ	10^{-3}	10^{-2}	10^{-1}	1	No Chem. Loss, $\gamma = 10^{-1}$
C/N	2.98	1.78	1.28	1.18	1.34
C/H	3.87	1.91	1.29	1.17	1.32
CPR	0.24	0.50	1.27	1.97	1.62

retrieved haze optical properties from the Cassini/Huygens mission and the observed geometric albedo.

4.1. Size distribution

The microphysical evolution of the produced monomers leads to the production of bigger size particles, the final size of which is constrained only by the electrostatic repulsion among them. The charging rate of the particles was kept constant during the calculations at $25\,e^-\,\mu m^{-1}$. Typical values for the charging rate, from previous microphysical models, range between 20 and $30\,e^-\,\mu m^{-1}$. Differences originate from the use of different shape particles, different production regions and different monomer sizes.

Based on the sensitivity analysis we performed for this parameter, the above value gave the best results regarding the agreement between the model and measured geometric albedo, while at the same time provided a spectral variation for the haze column opacity that is consistent with that observed by the DISR instrument (Tomasko et al., 2005), discussed later on. Higher (lower) values for the charging rate, constrain the final average size of the particles to smaller (bigger) values, which for a certain wavelength, decreases (increases) their efficiency factors, based on Mie theory. Hence, by decreasing the charging rate we increase the scattering of the aerosol particles and in this way enhance the geometric albedo above $0.6\,\mu m$, where the particles are mostly scattering rather than absorbing. The size distribution of the produced particles is presented in the contour plot of Fig. 15.

Since the model generates the population for each size particle, an optically effective radius at each altitude can be calculated. This average size of particles corresponds to the size that has the maximum effect in the radiation transfer calculations and is weighted according to the surface, S_i, of

each particle, i

$$R_{\mathrm{eff}} = \frac{\sum_i n_i r_i S_i}{\sum_i n_i S_i} = \frac{\sum_i n_i r_i^3}{\sum_i n_i r_i^2}. \qquad (2)$$

The resulting effective radius is presented also in Fig. 15 along with the range of values retrieved for this parameter by the Voyager measurements (Rages et al., 1983). Below 200 km, R_{eff} approaches a constant value of $0.2\,\mu m$ which is the lower limit value retrieved by these measurements. In addition this limiting optically effective size for the particles is identical with the equivalent sphere radius suggested by McKay et al. (2001) based on calculations performed with fractal particles.

4.2. Opacity and structure

Using the Khare et al. (1984) measurements for the refractive index, the opacity of the produced particles can be calculated with the use of Mie theory. The above measurements for the refractive index extend from UV to the IR and are the only ones published that cover such a long interval of the spectrum, which explains their use by all radiation transfer models so far. As discussed in Part I, the application of a scaling factor to the spectral variation of this refractive index was found to be necessary in order to obtain a reasonable match to the spectrally resolved geometric albedo and the vertical temperature structure. These scaling factors are used for the shortwave and thermal infrared haze properties involved in the radiation transfer. In the shortwave, the scaling controls the absorptivity of the particles and hence the match of the geometric albedo below $0.6\,\mu m$, where the refractive index shows significant absorption, and through this absorption the extent of the temperature rise in the stratosphere. In the thermal infrared it affects the efficiency of the cooling due to emission from the aerosol particles and hence directly the temperature structure. McKay et al. (1989) suggested a set of scaling factors ($\frac{4}{3}$ for solar and $\frac{1}{2}$ for thermal), which were retrieved based on an optimum match to the observed geometric albedo using spherical aerosol particles. Using their values we also find that the agreement for the temperature and geometric albedo is significantly improved and hence adopted them in the calculations. In other microphysical models in which fractal particles are used, a larger scaling has to be considered in order to match the geometric albedo (e.g. 2–2.3 for the solar spectrum as in Rannou et al., 2003).

The produced haze particles are assumed to be irreversibly lost to the surface through deposition. Yet, if no other loss process is included, large opacities are maintained in the lower atmosphere in a steady state. A parameter that affects the flow of the particles in this region is the mixing profile used. If the particles are assumed to be mixed with the same eddy coefficient as the gas molecules, then the resulting flux of particles towards the surface is small and the haze opacity builds up in the
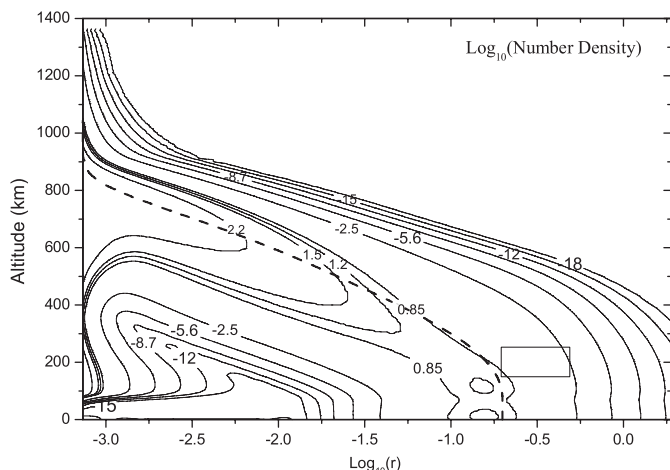

Fig. 15. Contour plot of the model size distribution for the haze particles. Size is in microns and number density is in cm^{-3}. The dashed line corresponds to the optically effective average radius for this distribution of sizes and the rectangle gives the range of values for the effective size of the particles retrieved by Rages et al. (1983) from the Voyager I measurements.

lower atmosphere. This is significantly different from that measured by the DISR instrument on board the Huygens probe and also much larger than the opacity necessary to match the geometric albedo and the vertical temperature structure. Previous radiation transfer models have also noticed this problem and solved it by applying a cut-off in the haze extinction profile in order to match the observed geometric albedo. The shape and magnitude of this reduction varies among different models, between total removal of the haze opacity below a certain altitude (McKay et al., 1989; Tomasko et al., 1997) or decreased opacity in a certain region (Rannou et al., 2003). But the latest results of the DISR instrument have shown that the haze extends down to the surface with a rather constant opacity below 100 km.

In view of these results we have attempted a different approach, that of an increased mixing coefficient for the haze particles below the stratopause, relative to the one used for the gas species. This allows the particles to flow faster towards the surface where they are irreversibly lost. The mixing profile for the haze particles above the stratopause is considered to be the same as for the rest of the chemical species in the model. The magnitude of the mixing below the stratopause was increased until a good match to the geometric albedo was obtained. After scaling the mixing in this way we realized that the resulting mixing profile between 300 and 100 km was very close to the mixing profile obtained assuming an altitude dependence that follows the inverse square root of the density ($\rho^{-1/2}$) scaled to the mixing magnitude at 300 km. Due to the close agreement between the vertical mixing profile needed to match the geometric albedo and the scaling suggested by the above dependence we have adopted it in the calculations. This approach for the scaling of the mixing profile of the particles was suggested by previous microphysical models (Rannou et al., 2003) and references therein, although the magnitude of the mixing coefficient varies among models.

Below 100 km the eddy mixing profile derived with the above process shows a sharp decrease due to the increase in the density below that level, which is related to the sharp decrease in the temperature observed in this region. Allowing for such a mixing profile still results in a haze opacity which is too large. Hence, we have assumed increased mixing in the lower 80 km, relative to that following $\rho^{-1/2}$. The eddy mixing profile used in the calculations is presented in Fig. 16.

This increased flux towards the surface sink is just a simulation of a loss process taking place in Titan's atmosphere. In the lower atmosphere below the stratopause, hydrocarbons and nitriles condense and are removed from the atmosphere. Cloud formation has been observed in specific locations on Titan's disk (Porco et al., 2005; Griffith et al., 2005, 2006; Roe et al., 2005; Hirtzig et al., 2006), while Rannou et al. (2006) have shown that the production of clouds using the haze particles as nucleation sites, is possible in certain latitudinal regions,
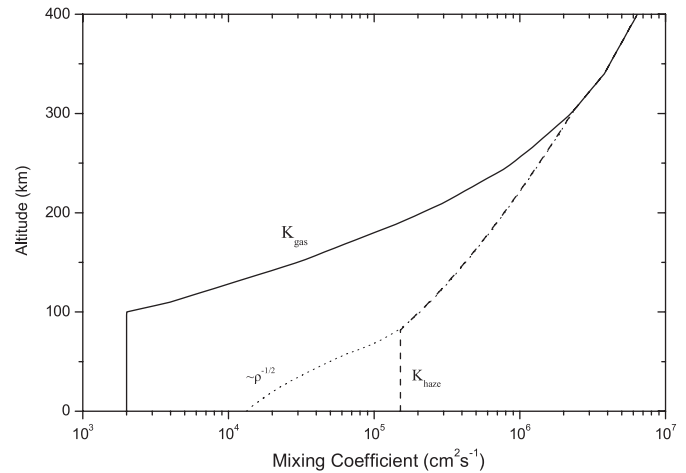

Fig. 16. The eddy mixing profile used for the aerosol particles. The solid line corresponds to the mixing profile used for the gas species, while the dotted line presents the mixing profile assuming an altitude dependence that follows the $\rho^{-1/2}$ law starting at 300 km. The dashed line presents the final mixing profile used for the haze particles, where in the lower 80 km the mixing magnitude has been increased in order to enhance the loss of the particles to the surface.
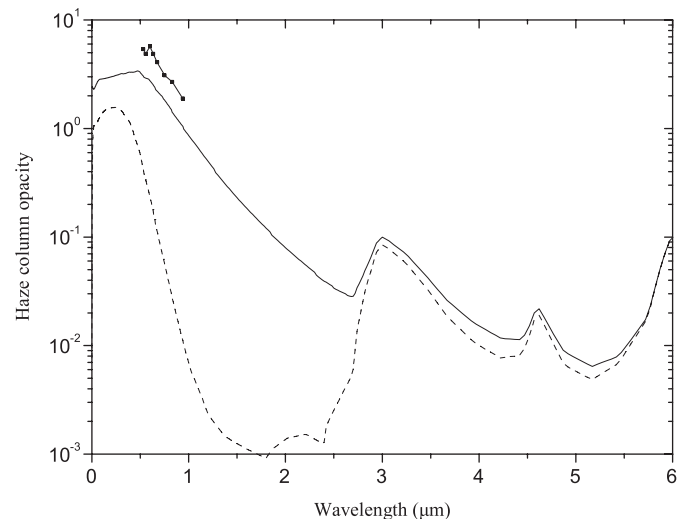

Fig. 17. The column absorption (dashed line) and extinction (solid line) opacity for the produced haze particles based on the model calculations, along with the measured extinction by the DISR instrument on board the Huygens probe (Tomasko et al., 2005). The particles were considered to attain a spherical shape (Mie particles) and the refractive index required for the calculation of the efficiencies was taken from the laboratory simulations of Khare et al. (1984).

similar to the ones were clouds are observed. Hence the condensation of atmospheric gases with the consequent cloud formation acts as a sink for the haze particles, which could explain the haze opacity in this region. Applying a large eddy mixing coefficient is just a way of representing this loss, by making the particles flow faster towards the surface sink. Further, the larger eddy mixing profile assigned for the haze particles in the lower atmosphere, below the stratopause, compared to that for the gas species, is found to be necessary irrespective of the value assumed

for the γ parameter (Eq. (1)). The results presented in Table 5 correspond to the eddy mixing profile shown in Fig. 16.

The resulting column haze opacity is presented in Fig. 17 and compared with the measured values retrieved by the DISR instrument (Tomasko et al., 2005). It must be kept in mind that the latter correspond to the location where the probe descended, while the model results correspond to the disk-average opacity that is necessary to provide a good match to the geometric albedo and a realistic temperature profile corresponding to global average conditions. Our model calculations suggest that a smaller total haze opacity than the measured one is more appropriate in order to match the observations. The measured column opacity by DISR at 750 nm, is 70% larger than the one retrieved by matching the observed geometric albedo (Fig. 19). Nevertheless, the measured spectral variation of the opacity between 531 and 938 nm, is similar to that of the model based on the refractive index assumed (Khare et al., 1984) and the charging rate value used in the calculations. For the moment we have not tried to use other published refractive indexes.

The DISR measurements have also provided results regarding the vertical variation of the haze opacity. The extinction profiles measured cover the above reported range and a comparison between the locally measured and disk-average model profiles, is presented in Fig. 18, for four wavelengths. Similar results were obtained for other wavelengths given by DISR. Although the DISR extinction profiles were retrieved assuming the particles to have a fractal structure, the resulting opacity is not depended on the shape of the particles. The DISR instrument measures the variation in the radiation intensity between layers of the atmosphere and hence retrieves the opacity necessary for the reproduction of this variation with altitude. Whether the particles are of spherical or fractal shape, this will have an impact on the resulting number density and size distribution of the particles.

The vertical variation of the opacity derived by the model calculations based on the suggested pathways is very close to that observed by the DISR measurements. The copolymer contribution in the upper atmosphere is mainly responsible for the production of particles, the evolution of which provides the opacity in the region above 300 km. Without the contribution from this family the haze structure would be significantly different with smaller extinction values. At lower altitudes the cumulative contribution from aromatics and nitriles produces the observed opacity, which is constrained by the enhanced mixing applied.

At higher altitudes the model-derived extinction profiles decrease faster than the observed profiles. This is the manifestation of dynamical effects, which become important in this region leading finally to the production of the observed detached haze layers. Under the current picture of haze formation, it is evident that the chemical composition of the detached haze layer will be mostly affected by the copolymer family than by the nitriles/aromatics, which are formed further below. This could lead to different optical properties for the particles formed in this region compared to the optical properties of the final particles in the lower atmosphere. Such a qualitative picture was obtained also by Rannou et al. (2000) in their investigation of the detached haze optical properties.

4.3. Geometric and surface albedo

The agreement between model and observed geometric albedo is an important validation parameter, since it provides a picture for the whole atmospheric structure and composition. Different energy photons reach different
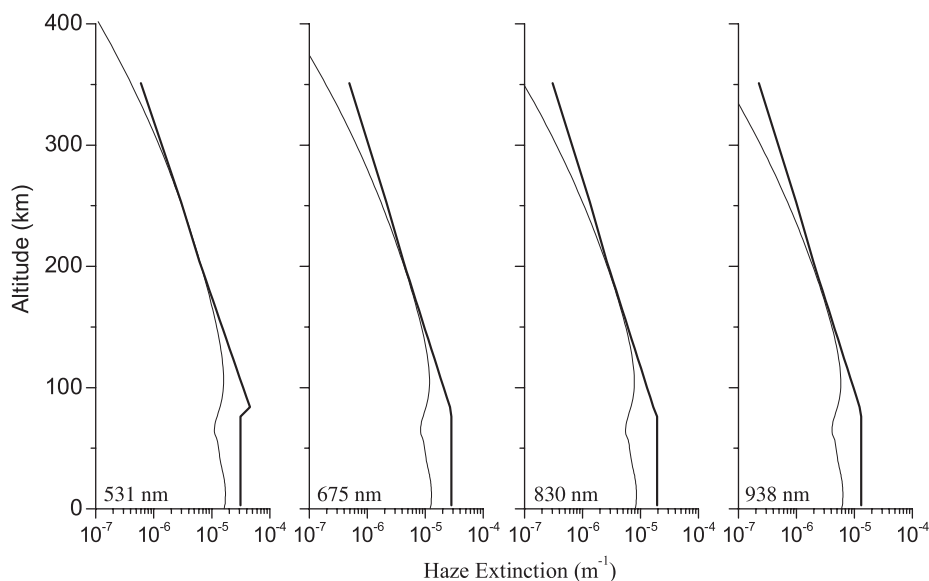

Fig. 18. The disk average resulting extinction profiles of the haze particles at different wavelengths compared with the DISR retrieved profiles which are characteristic of the Huygens probe descent location.

altitudes of the atmosphere, hence the spectrally resolved geometric albedo depends on the haze structure, the chemical composition and the surface albedo. The model geometric albedo is presented in Fig. 19 where it is compared with measurements from HST in the UV region between 1800 and 3300 Å (McGrath et al., 1998), the Neff et al. (1984) (0.35–1.05 μm) and Karkoschka (1994) (0.30–1.0 μm) measurements in the visible and near infrared, along with the Negrão et al. (2006) (0.8–2.5 μm), Geballe et al. (2003) (2.9–3.5 μm) and Coustenis et al. (2003) (2.6–4.8 μm) measurements in the above intervals. Also in the lower panel of Fig. 19, the corresponding lowest altitude at which photons at each wavelength reach inside the atmosphere is presented. This is calculated in terms of the effective optical depth:

$$\tau_{eff} = \tau\sqrt{(1-\omega)(1-\omega g)} \qquad (3)$$

with ω the single scattering albedo and g the asymmetry factor. The effective optical depth, τ_{eff}, provides a better estimate for the penetration depth of photons inside the atmosphere since it includes the contribution of the forward scattered photons (Rannou et al., 2003).

The agreement between the model and observed geometric albedo in the UV region is significantly improved compared to previous radiation transfer models that used haze opacities derived for spherical particles. The reason for this better agreement is the more complete description of the atmospheric composition in the radiation transfer calculations, with the inclusion of the absorption cross sections of all the photodissociated species used in the photochemical description. The altitude of penetration for UV photons decreases with increasing wavelength. Photons with energies below 100 nm are absorbed at altitudes above

1000 km, while between 100 and 200 nm the altitude of penetration exhibits a sharp decrease, reaching about 135 km at 200 nm. Between 200 and 300 nm the altitude of penetration has a small plateau. This is also observed in the geometric albedo in this region, which is approaching a constant value although measurements suggest that there is a steady decrease of the observed geometric albedo towards smaller wavelengths (McGrath et al., 1998). This could be an indication of missing gas absorption by species not included in the calculations, or of increased absorptivity of the haze particles in this spectral region, but most likely a signature of the contribution of the detached haze layer.

In the visible part of the spectrum the model provides a very good match to the observed geometric albedo. In this region the opacity is mainly controlled by haze absorption, which decreases as we move to larger wavelengths. Hence the altitude of penetration has an equivalent drop. In the region of 0.64 μm, the calculated geometric albedo, matches very well the observed minimum due to methane absorption. This is a common characteristic for spherical haze particles in contrast to fractal. The correct fit of the geometric albedo in the visible part of the spectrum, where the particles are mainly absorbing suggests a correct representation of the main haze layer by the model haze structure.

At longer wavelengths, the spectrum is characterized by the strong minima produced by the methane absorption bands. The contribution of haze, which is mostly scattering now, mainly controls the magnitude of the geometric albedo inside and on the sides of the methane windows that corresponding to the peaks. Inside the windows, photons can reach the surface where the reflected flux depends significantly on the surface albedo. The spectral variation
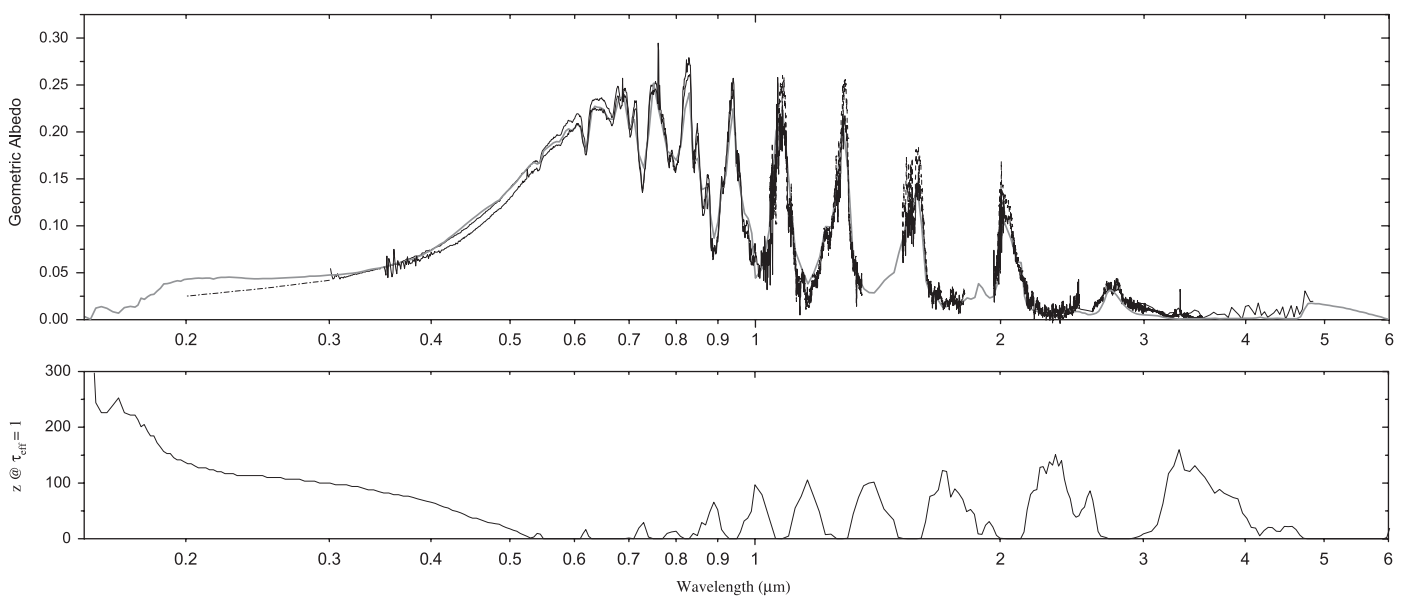

Fig. 19. Top panel: observed and modelled geometric albedo of Titan's atmosphere. Observed values are taken from Neff et al. (1984) (0.35–1.05 μm), Karkoschka (1994) (0.30–1.0 μm), Negrão et al. (2006) (0.8–2.5 μm), Geballe et al. (2003) (2.9–3.5 μm) and Coustenis et al. (2003) (2.6–3 μm), while the dash-dotted line between 0.2 and 0.3 μm, represents the McGrath et al. (1998) measurements. Dashed and solid lines at similar wavelengths correspond to the leading and trailing hemispheres, respectively. Bottom panel: depth of penetration of photons inside the atmosphere.
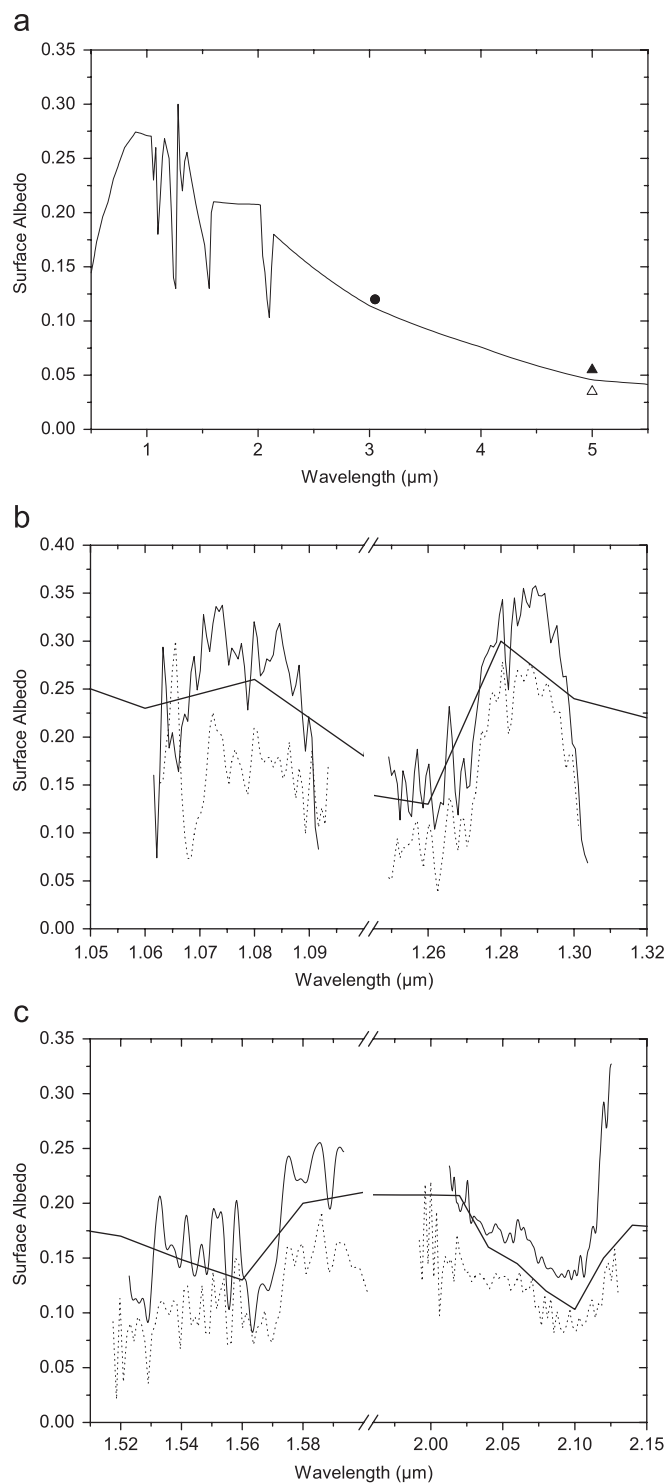
of surface reflectivity used is shown in Fig. 20(a) and is in between the surface albedos reported by Negrão et al. (2006), in the interval 1.06–2.12 µm (see Fig. 20(b,c)), for the leading and trailing sides of Titan's atmosphere. As discussed in Part I, we have used the Boudon et al. (2004) line by line absorption coefficients for methane in the near IR above 1.54 µm, as Negrão et al. (2006) did, which explains the agreement between the surface albedo values presented here and the ones reported by the latter authors, compared to previous results (Griffith et al., 2003) based on different absorption calculations for methane. At longer wavelengths the values for the surface albedo were constrained to be close to those reported by Coustenis et al. (2006) at 3 µm and Lellouch et al. (2004) at 5 µm.

5. Atmospheric structure

Having provided a description of the haze optical properties generated by the model calculations based on the photochemical description of the atmosphere and the suggested pathways of haze formation, we now present the resulting atmospheric structure that also controls the above processes. In the following paragraphs we present the calculated vertical temperature structure and atmospheric density and validate them against the retrieved values by the CIRS and HASI measurements.

The resulting temperature profile, based on the above description of haze production and evolution, is presented in Fig. 21 for the lower (a) and upper (b) atmosphere. For comparison the retrieved vertical temperature profiles from HASI (F. Ferri, private communication) and CIRS (R. Achterberg and B. Conrath, personal communication) are given. The bundle of CIRS profiles present the variation of the temperature structure at different latitudes from pole to pole. The variation of the temperature is rather small, only a few degrees for most latitudes until we start to move towards the winter pole where the stratopause temperature increases and the stratosphere below cools. This is related to the seasonal variation of the atmospheric structure that enhances the production of haze particles in the winter pole and hence produces this temperature variation. At higher altitudes, above the stratopause, the temperature profiles converge again, indicating that the atmosphere above is well mixed. It is important to note the different location for the stratopause and the stratospheric temperatures retrieved by the two instruments. The in situ measurements of HASI (which correspond to a specific pathway through Titan's atmosphere by the Huygens probe) suggest a hotter stratosphere compared to the average temperature retrieved by CIRS as described by the overlap of the mid-latitude and equatorial profiles in Fig. 21a. The location of the stratopause for HASI is at about 250 km with a temperature slightly above 185 K, while the CIRS profile provides a higher stratopause situated at 320 km with a few degrees colder temperature (at equatorial regions). The differences between the profiles derived by the two instruments have yet to be explained.

Fig. 20. (a) Spectral variation of the surface albedo used in the model (solid line). The circle at 3 µm is from Coustenis et al. (2006) while filled and empty triangles correspond to the surface albedo values from Lellouch et al. (2004) for the leading and trailing sides of Titan, respectively. (b) and (c) present the model surface albedo (thick solid line) inside the methane windows in the range 1.0–2.5 µm, compared to the values retrieved by Negrão et al. (2006) (thin solid and dotted line for the leading and trailing side, respectively.
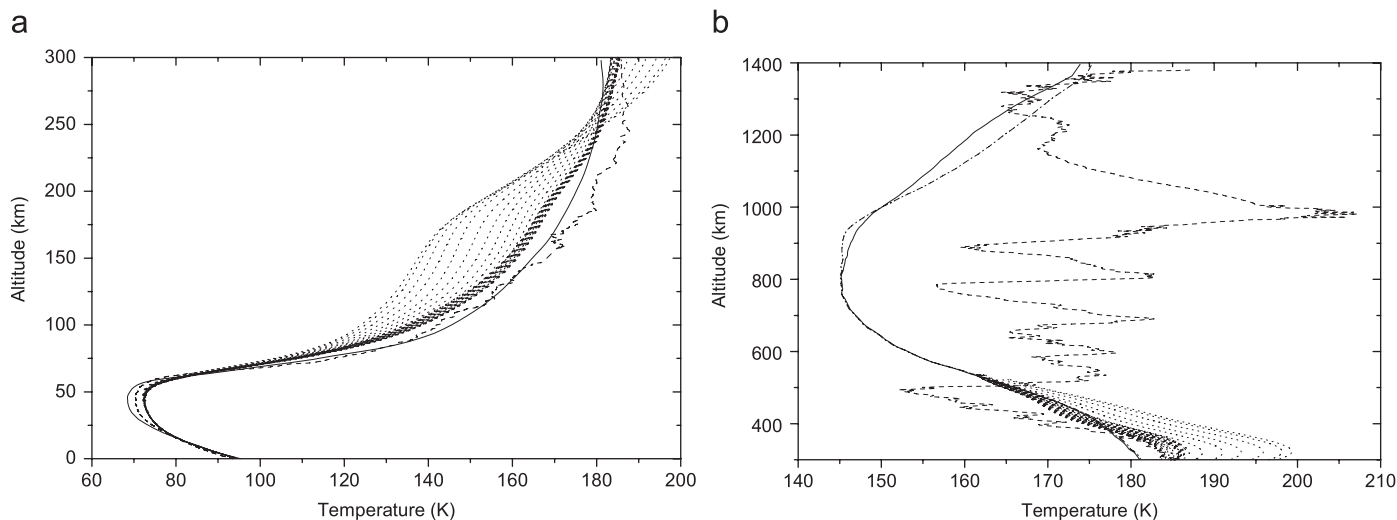
a

b

Fig. 21. Calculated vertical temperature profile and the retrieved temperature profiles of the HASI (Huygens) and CIRS (Cassini) instruments presented with dashed and dotted lines, respectively. In the lower atmosphere (a), the model agrees better with the HASI observed profile and provides a stratopause located at 280 km. In the upper atmosphere (b), above 375 km, the calculated profile converges with the majority of the CIRS measurements that constitute the thicker solid line, which represents overlapping of many profiles from mid-latitude and equatorial regions.

Our calculated vertical profile, which corresponds to global average conditions, provides an intermediate temperature structure between the observed profiles. It is in better agreement with the HASI profile in the lower atmosphere where it follows it closely up to ∼170 km. Above that region it provides a colder stratopause of about 182 K but located at 280 km in the same region as the HASI profile. At higher altitudes our temperature drops more slowly compared to the HASI and approaches the converging CIRS profiles above 375 km (Fig. 21b).

In the troposphere, as was shown by McKay et al. (1989), the greenhouse effect from the collision induced absorption controls the temperature structure. The thermal window in the region between 400 and 600 cm^{-1} which is controlled by the N_2–H_2 and H_2–CH_4 collision induced absorption, controls the thermal flux that can escape from the surface and troposphere to space. Hence, the correct simulation of the hydrogen budget affects the atmospheric temperature. In the lower atmosphere the H_2 mole fraction is constant. According to our calculations, increasing the H_2 mole fraction from 1×10^{-3} to 2×10^{-3} leads to an increase in the surface temperature by about $\frac{1}{2}$ a degree.

The rapid increase of the temperature profile above the tropopause, depends mainly on the structure of the haze extinction profile and hence on the correct representation of the main haze layer by the model.

Above the stratopause, IR cooling by methane, acetylene and ethane defines the extent of the temperature drop. The current calculations do not include corrections due to non-LTE effects. In the upper atmosphere, the HCN profile controls the thermospheric cooling due to transitions in the rotational degrees of freedom, which are in LTE under the conditions found in Titan's thermosphere (Yelle, 1991). Heating is provided by the UV photodissociation of the atmospheric species. As was shown, the model-generated

HCN profile is above the measured abundance in the upper atmosphere, where the effect of the HCN cooling has its maximum impact. This means that the modelled temperature profile is colder than what it should be if the HCN abundance was correctly reproduced. This underestimation of the temperature is also presented in Fig. 21b with the dashed-dotted line, where we have set an upper limit in the radiation transfer calculations for the calculated HCN mole fraction based on the derived values from the INMS measurements (2×10^{-4}, Vuitton et al., 2006a). The increase in the temperature is located above 900 km having reached a maximum of ∼5 K above 1200 km. This temperature difference did not provide any significant changes to the vertical profiles of the species in this region.

As discussed above, the model profile corresponds to a global average temperature structure. The observed profiles include the contribution of dynamical effects that produce variations in the vertical temperature structure. The latitudinal transport induced by the Hadley circulation allows the haze particles to remain in the atmosphere for a longer time until they are deposited in the polar regions, where the circulation fluxes attain a descending character. In our model we only simulate the vertical motion of the particles and hence we do not take into consideration this effectively smaller settling velocity of the particles, when viewed in a one-dimensional picture. On the other hand, the observed oscillations in the vertical temperature structure of the upper atmosphere by the HASI instrument, suggest the presence of significant transient wave effects which are not simulated by the model.

Another validation parameter is the vertical profile of the mass density. This was measured by the HASI instrument on board the Huygens probe during its descent inside Titan's atmosphere (Fulcignoni et al., 2005). The measured and modelled vertical profiles for this quantity
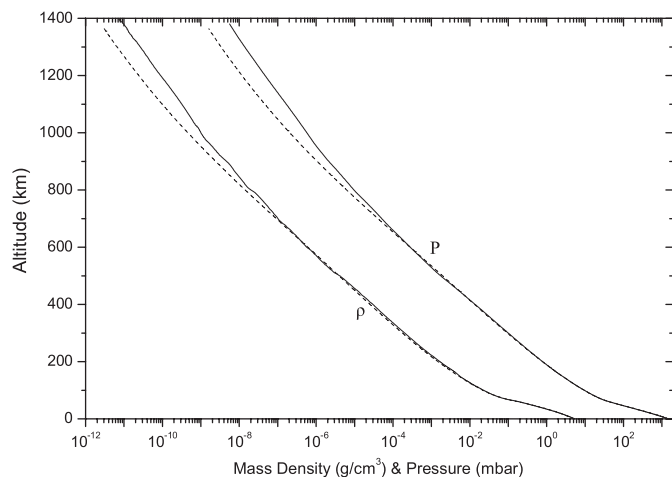
Fig. 22. The model vertical mass density and pressure profiles (dashed lines) compared with the observed profiles (solid lines) by the HASI instrument on board the Huygens probe (Fulcignoni et al., 2005).

are presented in Fig. 22. Mass density depends on the vertical temperature structure, which defines the atmospheric density, and the chemical composition of the atmosphere. From the surface up to about 800 km the modelled and observed density and pressure profiles are very close.

6. Discussion

The one-dimensional picture of Titan's atmospheric processes presented in this work has provided a realistic representation of the mean atmospheric structure and composition. The haze pathways used provide a haze production profile which can reproduce the observed aerosol structure by the DISR measurements. At the same time, the interaction of the calculated haze structure with the radiation field provides a vertical temperature profile which is in very good agreement with observations, while the very good agreement between the model spectrally resolved geometric albedo and the observed one, suggests a realistic representation of radiation transfer through Titan's atmosphere. The solar fluxes calculated by the model, along with the temperature structure, drive the photochemical and thermochemical evolution of the simulated species, for most of which the model provides reasonably good vertical profiles compared with the observations. Under this self-consistent picture where each process is linked to the others, a more complete representation of Titan's atmosphere has been presented and the effect of the coupling between different processes has been investigated.

6.1. Haze pathways and chemical loss

Amongst the pathways included in the description of the photochemical production of the haze particles, nitriles and copolymers have the most important role. Copolymers have a dominant contribution in the upper atmosphere and

are the main source for the opacity above the stratopause, which is necessary for the correct reproduction of the vertical temperature structure. When the impact of the galactic cosmic rays is included, nitriles contribute mainly in the lower atmosphere and are of secondary importance in the radiation transfer since the particles formed in this region are quickly lost to the surface. If the contribution of the GCR is removed, the haze production in the lower atmosphere is significantly reduced and is then controlled by the aromatics. The contribution from polyynes at all altitudes and under all conditions, is significantly smaller than that of the other families. Hence, under our description the omission of pure hydrocarbon pathways from the haze production, in accordance with the results of the ACP instrument, would not change the produced haze structure significantly. This altitude-dependent chemical composition of the haze particles is in agreement with the observed variation of the detached haze optical properties relative to the ones of the main haze layer, as reported by Rannou et al. (2000), although in the current calculation we have assumed a single refractive index for all altitudes.

The chemical loss of atmospheric gases through the formation of the haze monomers, is found to be important for the vertical profiles of the precursor species involved in the haze pathways used. The chemical growth of the initial dimer formed, to the size of a monomer, beyond which the particles become larger by their mutual coagulation, has the largest impact on the chemical composition. The increased contribution of hydrocarbon-nitrile copolymers and pure nitriles relative to the pure hydrocarbon pathways in the haze production results in a significant loss for nitrogen in all forms of nitrile species involved in the pathways.

The profiles of HCN, HC_3N and C_2H_3CN are reduced in the stratosphere, although the magnitude of this reduction depends mainly on the assumed rate for the reaction $H_2CN + HCN$. An important conclusion from the current work regarding this rate is that its variation, although affects significantly the HCN abundance and the total haze production in the stratosphere, has a very small impact on the resulting haze opacity. The calculated C/N and C/H ratios suggest a stoichiometric formula of $C_4H_3N_3$ for the haze particles.

6.2. N_2 dissociative photoionization and nitriles

Another sensitivity test from our work is the new dissociative ionization scheme for N_2 suggested by the work of Nicolas et al. (2003). Compared to previous suggestions that favored the production of ground state neutral and ionized nitrogen atoms for wavelengths smaller than 510 Å, the latter measurements suggest that the neutral atoms are in their excited state. The effect of this is to produce significantly larger CH_3CN abundance compared to the observed. For other species, such as HCN, CH_2NH, C_2H_6 and C_2H_2 the effect is smaller.

6.3. Heterogeneous chemistry

The current work has provided more insight into the effects of heterogeneous processes on the surface of aerosol particles. The scavenging of atomic hydrogen and its conversion to molecular hydrogen by aerosols results in a H_2 vertical profile closer to that retrieved by INMS in the upper atmosphere. It also produces a vertical diacetylene profile that is in much better agreement with the CIRS retrieved profiles. Further, it affects the radiation transfer; first, directly due to the higher abundance of diacetylene, and secondly indirectly, since C_4H_2 is a very important precursor for haze production based on the copolymer family. Another important process is the increased thermal opacity inside the thermal window between 400 and $600\,cm^{-1}$ because of H_2–N_2 and H_2–CH_4 collisionally induced absorption that arises from increased H_2 abundance. This allows less of the thermal radiation to escape to space and hence increases the surface temperature. It is clear that heterogeneous processes affect the temperature, radiation field, photochemistry and haze production.

6.4. The role of methyl radicals

Methyl radicals play an important role in the photochemical evolution of the atmosphere. As discussed in the previous sections, their recombination defines the production of C_2H_6, while reaction with atomic nitrogen is the main production mechanism for HCN and CH_2NH. In addition, their photolysis is a significant source of $^1CH_2$ that affects the rest of the hydrocarbon chemistry. Hence variations in the abundance of CH_3 will have an impact on all of the above species. Both hydrogen cyanide and methyleneimine are overestimated by the model in the upper atmosphere. The model ethane (along with argon) profile is used for the retrieval of the eddy mixing profile, which depends on the methyl radical abundance.

Methyl radicals, like atomic hydrogen, can react heterogeneously with hydrogen atoms on the surface of the aerosol particles to form CH_4. If this process is of comparable efficiency with that observed for the conversion of H to H_2, the population of CH_3 radicals would be reduced with the process having its maximum effect in the region between 300 and 600 km, as observed for atomic hydrogen. This is the region where the eddy mixing profile is controlled by ethane. The possible reduction of the methyl radical by a heterogeneous process would lead to a decrease in ethane production within this region and hence to a different characteristic life time for this species relative to the one given in Fig. 1. Hence, variations in the eddy mixing profile would occur, while the reduced CH_3 abundance will have a photochemical effect on those species directly affected by it.

7. Conclusions

We have developed a one-dimensional radiative/convective–photochemical– microphysical model to study the formation of Titan's haze from the chemical species formed in its atmosphere. Our model results were validated against recent Cassini/Huygens mission measurements and other ground-based and space-borne observations. The model generates the radiation field, atmospheric composition, haze structure, geometric albedo and temperature/density structure in a self consistent manner.

More specifically, we have in this work used ethane and argon, and methane escape to space, to constrain the eddy mixing coefficient for the gaseous species, and have used a separate eddy mixing coefficient for the haze particles. The use of two different profiles was found to give better results with regard to the agreement between model and observed gaseous species vertical profiles of abundance and haze properties. Yet, the increased mixing profile assumed for the haze particles is just one way for constraining the produced haze abundance to the value that is necessary for the correct reproduction of the geometric albedo. The physical interpretation of this approach has to be clarified with further investigation. Possibly the loss of haze particles as nucleation sites upon which cloud formation can proceed can produce the same effect as the increased flow towards the surface sink applied here. Further, the latitudinal transportation of particles could effectively act in the same way, depositing the particles in the polar regions. On the other hand this could also signify some lack in our understanding of the chemical processes that define haze formation in Titan's atmosphere.

In our model calculations we have included the effects of the heterogeneous chemistry on aerosol surfaces that convert atomic hydrogen to molecular hydrogen. The resultant H_2 profile is found to be closer to the INMS measurements, while the vertical profile of the diacetylene formed, which is controlled by atomic hydrogen and the retrieved mixing profile, is found to be closer to that of the CIRS profile when this heterogenous chemistry is included. Both of these species play an important role in the radiative transfer; H_2 in collisionally induced absorption in the thermal infrared, and C_4H_2 in haze production based on the copolymer family.

We also present first results on the photochemistry of methyleneimine in Titan's atmosphere and compare our vertical profile with the INMS single measurement at 1100 km.

Our haze model reveals a new second major peak in the vertical profile of haze production rate between 500 and 900 km. This peak is produced by the copolymer family used and has important ramifications for the vertical atmospheric temperature profile and geometric albedo. In particular, the existence of this second peak determines the vertical profile of haze extinction. Our model results have been compared with the DISR retrieved profiles and are found to be in very good agreement, given that our results represent global mean values whereas the DISR represent profiles from the descent site of the Huygens probe. If this second peak is absent, then the model haze extinction profiles would decrease more rapidly above 100 km than

indicated by the DISR measurements. Further, this peak controls the atmospheric temperature decrease above 300 km.

Our model temperature profile is found to be in agreement with the HASI measurements in the lower atmosphere below the stratopause. The latter, based on our calculations is placed at 280 km. Above 375 km, the calculated temperature profile agrees better with the mid-latitude CIRS profiles. At higher altitudes, where the profiles from all latitudes begin to converge, the simulated and observed profiles are in agreement.

Finally, our model geometric albedo, which represents an integration of radiative processes in Titan's atmosphere is in very good agreement with the observations. The peaks in the near infrared are primarily controlled by haze scattering and surface albedo, whilst the troughs are determined by methane absorption. The matching of our model peaks and troughs with the observations lends further support to our coupling of Titan's photochemistry to haze formation.

Acknowledgments

References

Adachi, H., Basco, N., James, D.G.L., 1980. Mutual interaction of methyl and methylperoxy radicals studied by flash photolysis and kinetic spectroscopy. Int. J. Chem. Kinet. 12, 949–977.

Atreya, S.K., Edgington, S.G., Encrenaz, T., Feuchtgruber, H., 1999. ISO observations of C_2H_2 on Uranus and CH_3 on Saturn: implications for atmospheric vertical mixing in the Voyager and ISO epochs, and a call for relevant laboratory measurements. Eur. Space Agency Spec. Publ. ESA SP-427, 149–152.

Bakes, E.L.O., Lebonnois, S., Bauschlicher Jr., C.W., McKay, C.P., 2003. The role of submicrometer aerosols and macromolecules in H_2 formation in the Titan haze. Icarus 161, 468–473.

Balucani, N., Casavecchia, P., 2006. Laboratory studies on $N(^2D)$ reactions of relevance to the chemistry of planetary atmospheres. First European Planetary Science Congress 2006, P0162, EPSC2006-A-00079.

Balucani, N., Cartechini, L., Alagia, M., Casavecchia, P., Volpi, G.G., 2000a. Observation of nitrogen-bearing organic molecules from reactions of nitrogen atoms with hydrocarbons: a crossed beam study of $N(^2D)$ + ethylene. J. Phys. Chem. 104, 5655–5659.

Balucani, N., Asvany, O., Chang, A.H.H., Lin, S.H., Lee, Y.T., Kaiser, R.I., Osamura, Y., 2000b. Crossed beam reaction of cyano radicals with hydrocarbon molecules. III. Chemical dynamics of vinylcyanide (C_2H_3CN; X ^{1}A') formation from the reaction of $CN(X\ ^2\Sigma^+)$ with ethylene, $C_2H_4(X\ ^1A_g)$. J. Chem. Phys. 113, 8643–8655.

Basiuk, V.A., 2001. Formation of amino acid precursors in the interstellar medium. A DFT study of some gas-phase reactions starting with methyleneimine. J. Phys. Chem. A. 105, 4252–4258.

Baulch, D.L., Cobbs, C.J., Cox, R.A., Esser, C., Frank, P., Just, Th., Kerr, J.A., Pilling, M.J., Troe, J., Walker, R.W., Warnatz, J., 1992. Evaluated kinetic data for combustion modeling. J. Phys. Chem. Ref. Data 21, 411–734.

Bézard, B., Marten, A., Paubert, G., 1993. Detection of acetonitrile on Titan. Bull. Am. Astron. Soc. 25, 1100.

Bézard, Feuchtgruber, H., Moses, J.I., Encrenaz, T., 1998. Detection of methyl radicals (CH_3) on Saturn. Astron. Astrophys. 334, L41–L44.

Bocherel, P., Herbert, L.B., Rowe, B.R., Sims, I.R., Smith, I.W.M., Travers, D., 1996. Ultralow-temperature kinetics of CH(X2II) reactions: rate coefficients for reactions with O_2 and NO (T = 13−708 K), and with NH_3 (T = 23−295 K). J. Phys. Chem. 100, 3063–3069.

Boudon, V., Champion, J.-P., Gabard, T., Loëte, M., Michelot, F., Pierre, G., Rotger, M., Wenger, Ch., Rey, M., 2004. Symmetry-adapted tensorial formalism to model rovibrational and rovibronic spectra of molecules pertaining to various point groups. J. Mol. Spectrosc. 228, 620–634.

Callear, A.B., Metcalfe, M.P., 1976. Oscillator strengths of the bands of the $\tilde{B}^2A_1'$-$\tilde{X}A_2''$ system of CD_3 and a spectroscopic measurement of the recombination rate. Comparison with CH_3. Chem. Phys. 14, 275–284.

Choi, N., Blitz, M.A., McKee, K., Pilling, M.J., Seakins, P.W., 2004. H atom branching ratios from the reactions of CN radicals with C_2H_2 and C_2H_4. Chem. Phys. Lett. 384, 68–72.

Clarke, D.W., Ferris, J.P., 1997. Titan Haze: structure and properties of the cyanoacetylene and cyanoacetylene-acetylene photopolymers. Icarus 127, 158–172.

Cody, R.J., Romani, P.N., Nesbitt, F.L., Iannone, M.A., Tardy, D.C., Stief, L.J., 2003. Rate constant for the reaction $CH_3 + CH_3 \rightarrow C_2H_6$ at T = 155 K and model calculation of the CH_3 abundance in the atmospheres of Saturn and Neptune. J. Geophys. Res. 108.

Coustenis, A., Bézard, B., 1995. Titan's atmosphere from Voyager infrared observations. IV. Latitudinal variations of temperature and composition. Icarus 115, 126–140.

Coustenis, A., Salama, A., Schulz, B., Ott, S., Lellouch, E., Encrenaz, Th., Gautier, D., Feuchtgruber, H., 2003. Titan's atmosphere from ISO mid-infrared spectroscopy. Icarus 161, 383–403.

Coustenis, A., Negrão, A., Salama, A., Schulz, B., Lellouch, E., Rannou, P., Drossart, P., Encrenaz, T., Schmitt, B., Boudon, V., Nikitin, A., 2006. Titan's 3-micron spectral region from ISO high-resolution spectroscopy. Icarus 180, 176–185.

Coustenis, A., and 24 co-authors, 2007. The composition of Titan's stratosphere from Cassini/CIRS mid-infrared spectra. Icarus, in press.

Duley, W.W., 1996. The formation of H_2 by H-atom reaction with grain surfaces. Monthly Notices Royal Astron. Soc. 279, 591–594.

Fulcignoni, M., and 42 coworkers, 2005. In situ measurements of the physical characteristics of Titan's environment. Nature, doi:10.1038/nature04314.

Geballe, T.R., Kim, S.J., Noll, K.S., Griffith, C.A., 2003. High-resolution 3 micron spectroscopy of molecules in the mesosphere and troposphere of Titan. Astrophys. J. 583, L39–L42.

Griffith, C.A., Owen, T., Geballe, T.R., Rayner, J., Rannou, P., 2003. Evidence for the exposure of water ice on Titan's surface. Science 300, 628–630.

Griffith, C.A., and 26 co-workers, 2005. The evolution of Titan's mid-latitude clouds. Science 310, 474–477.

Griffith, C.A., and 13 co-workers, 2006. Evidence for a polar ethane cloud on Titan. Science 313, 1620–1622.

Gurwell, M., 2004. Submillimeter observations of Titan: global measures of stratospheric temperature CO, HCN HC_3N and the isotopic ratios $^{12}C/^{13}C$ and $^{14}N/^{15}N$. Astrophys. J. 616, L7–L10.

Herron, J.T., 1999. Evaluated chemical kinetics data for reactions of N(^{2}D), N(^{2}P), and N$_2$(A$^3\Sigma_u^+$) in the gas phase. J. Phys. Chem. Ref. Data 28, 1453–1483.

Hidayat, T., Marten, A., Bézard, B., Gautier, D., Owen, T., Matthews, H.E., Paubert, G., 1997. Millimeter and submillimeter heterodyne observations of Titan: retrieval of the vertical profile of HCN and the ^{12}C/^{13}C ratio. Icarus 126, 170–182.

Hirtzig, M., Coustenis, A., Gendron, E., Drossart, P., Negrao, A., Combes, M., Lai, O., Rannou, P., Lebonnois, S., Luz, D., 2006. Monitoring atmospheric phenomena on Titan. Astron. Astrophys. 456, 761–774.

Horne, D.G., Norrish, R.G.W., 1970. The photolysis of acyclic azines and the electronic spectra of R$_1$R$_2$CN radicals. Proc. R. Soc. London A 315.

Hourdin, F., Lebonnois, S., Luz, D., Rannou, P., 2004. Titan's stratospheric composition driven by condensation and dynamics. J. Geophys. Res. 109.

Israël, G., and 21 co-authors, 2005. Complex organic matter in Titan's atmospheric aerosols from *in situ* pyrolysis and analysis. Nature doi:10.1038/nature04349.

Karkoschka, E., 1994. Spectrophotometry of the jovian planets and Titan at 300 to 1000 nm wavelength: the methane spectrum. Icarus 111, 174–192.

Kassner, Ch., Stuhl, F., 1994. The VUV photodissociation CH$_3$ → CH(A$^2\Delta$ and B$^2\Sigma^-$) + H$_2$. Chem. Phys. Lett. 222, 425–430.

Khare, B.N., Sagan, C., Arakawa, E.T., Suits, F., Calcott, T.A., Williams, M.W., 1984. Optical constants of organic tholins produced in a simulated Titanian atmosphere: from soft X-ray to microwave frequencies. Icarus 60, 127–137.

Knyazev, V.D., Slagle, I.R., 2001. Kinetics of the reactions of n-Alkyl (C$_2$H$_5$, n-C$_3$H$_7$, and n-C$_4$H$_9$)radicals with CH$_3$. J. Phys. Chem. A 105, 6490–6498.

Lara, L.-M., Lellouch, E., Lopez-Moreno, J., Rodrigo, R., 1996. Vertical distribution of Titan's atmospheric neutral constituents. J. Geophys. Res. 101, 23261–23283.

Lara, L.-M., Lellouch, E., Shematovich, V., 1999. Titan's atmospheric haze: the case for HCN incorporation. Astron. Astrophys. 341, 312–317.

Lebonnois, S., 2005. Benzene and aerosol production in Titan and Jupiter's atmospheres: a sensitivity study. Planet. Space Sci. 53, 486–497.

Lebonnois, S., Bakes, E.L.O., McKay, C.P., 2002. Transition from gaseous compounds to aerosols in Titan's atmosphere. Icarus 159, 505–517.

Lebonnois, S., Bakes, E.L.O., McKay, C.P., 2003. Atomic and molecular hydrogen budget in Titan's atmosphere. Icarus 161, 474–485.

Lellouch, E., Romani, P.N., Posenqvist, J., 1994. The vertical distribution and origin of HCN in Neptune's atmosphere. Icarus 108, 112–136.

Lellouch, E., Schmitt, B., Coustenis, A., Cuby, J.-G., 2004. Titan's 5-micron lightcurve. Icarus 168, 209–214.

Marten, A., Hidayat, T., Biraud, Y., Moreno, R., 2002. New millimeter heterodyne observations of Titan: vertical distributions of HCN HC$_3$N, CH$_3$CN, and the isotopic ratio ^{15}N/^{14}N in its atmosphere. Icarus 158, 532–544.

McGrath, M.A., Courtin, R., Smith, T., Feldman, P.D., Strobell, D.F., 1998. The ultravionet albedo of Titan. Icarus 131, 382–392.

McKay, C.P., 1996. Elemental composition, solubility, and optical properties of Titan's organic haze. Planet. Space Sci. 44, 741–747.

McKay, C.P., Pollack, J.B., Courtin, R., 1989. The thermal structure of Titan's atmosphere. Icarus 80, 23–53.

McKay, C.P., Coustenis, A., Samuelson, R.E., Lemmon, M.T., Lorenz, R.D., Cabane, M., Rannou, P., Drossart, P., 2001. Physical properties of the organic aerosols and clouds on Titan. Planet. Space Sci. 49, 79–99.

Monks, P.S., Romani, P.N., Nesbitt, F.L., Scanlon, M., Stief, L.J., 1993. The kinetics of the formation of nitrile compounds in the atmosphere of Titan and Neptune. J. Geophys. Res. 98, 17115–17122.

Morter, C.L., Farhat, S.K., Adamson, J.D., Glass, G.P., Curl, R.F., 1994. Rate constant measurement of the recombination reaction C$_3$H$_3$ + C$_3$H$_3$. J. Phys. Chem. 98, 7029–7035.

Moses, J.I., Bézard, B., Lellouch, E., Gladstone, G.R., Feuchtgruber, H., Allen, M., 2000. Photochemistry of Saturn's atmosphere: I hydrocarbon chemistry and comparisons with ISO observations. Icarus 143, 244–298.

Münzel, N., Schweig, A., 1988. UV/VIS absorption spectrum, geometry and electronic structure of transient *o*-Benzyne. Chem. Phys. Lett. 147, 192–194.

Neff, J.S., Humm, D., Bergstralh, J.T., Cochran, A.L., Cochran, W.D., Barker, E.S., Tull, R.G., Absolute spectrophotometry of Titan, Uranus, and Neptune 3500-10,500 Å. Icarus 60, 221–235.

Negrão, A., Coustenis, A., Lellouch, E., Maillard, J.-P., Rannou, P., Schmitt, B., McKay, C.P., Boudon, V., 2006. Titan's surface albedo variations over a Titan season from near-infrared CFHT/FTS spectra. Planet. Space Sci. 54, 1225–1246.

Nguyen, M.T., Sengupta, D., Ha, T.-K., 1996. Another look at the decomposition of methyl azide and methanimine: How is HCN formed? J. Phys. Chem. 100, 6499–6503.

Nicolas, C., Alcaraz, C., Thissen, R., Vervloet, M., Dutuit, O., 2003. Dissociative photoionization of N$_2$ in the 24–32 eV photon energy range. J. Phys. B: At. Mol. Phys. 36, 2239–2251.

Niemann, H.B., and 17 co-authors, 2005. The abundance of constituents of Titan's atmosphere from the GCMS instrument on the Huygens probe. Nature doi:10.1038/nature04122.

Nizamov, B., Dagdigian, P.J., 2003. Spectroscopic and kinetic investigation of methylene amidogen by cavity ring-down spectroscopy. J. Phys. Chem. A 107, 2256–2263.

Parker, J.K., Payne, W.A., Cody, R.J., Stief, L.J., 2004. Kinetics of the reaction of atomic hydrogen with cyanoacetylene from T = 200 to 298 K. J. Phys. Chem A 108, 1938–1945.

Parkes, D.A., Paul, D.M., Quinn, C.P., Robson, R.C., 1973. The ultraviolet absorption by alkylperoxy radicals and their mutual reactions. Chem. Phys. Lett. 23, 425–429.

Payne, W.A., Monks, P.S., Nesbitt, F.L., Stief, L.J., 1996. The reaction between N(^{4}S) and C$_2$H$_3$: rate constant and primary reaction channels. J. Chem. Phys. 104, 9808–9815.

Pilling, M.J., Bass, A.M., Braun, W., 1971. Oscillator strengths of CH$_2$ and CH$_3$ in the vacuum ultraviolet. Chem. Phys. Lett. 9, 147–148.

Porco, C.C., and 35 co-workers, 2005. Imaging of Titan from Cassini spacecraft. Nature 434, 159–168.

Rages, K., Pollack, J.B., Smith, P.H., 1983. Size estimate of Titan's aerosols based on Voyager high-phase-angle images. J. Geophys. Res. 88, 8721–8728.

Rannou, P., Ferrari, C., Rages, K., Roos-Serote, M., Cabane, M., 2000. Characterization of aerosols in the detached haze layer of Titan. Icarus 147, 267–281.

Rannou, P., McKay, C.P., Lorenz, R.D., 2003. A model of Titan's haze of fractal aerosols constrained by multiple observations. Planet. Space Sci. 51, 963–976.

Rannou, P., Montmessin, F., Hourdin, F., Lebonnois, S., 2006. The latitudinal distribution of clouds on Titan. Science 311, 201–204.

Redondo, P., Pauzat, F., Ellinger, Y., 2006. Theoretical survey of the NH + CH$_3$ potential energy surface in relation to Titan atmospheric chemistry. Planet. Space Sci. 54, 181–187.

Roe, H.G., Greathouse, T.K., Richter, M.J., Lacy, J.H., 2003. Propane on Titan. Astrophys. J. 597, L65–L68.

Roe, H.G., Bouchez, A.H., Trujillo, C.A., Schaller, E.L., Brown, M.E., 2005. Discovery of temperate latitude clouds on Titan. Astrophys. J. 618, L49–L52.

Sato, K., Misawa, K., Kobayashi, Y., Matsui, M., Tsunashima, S., Kurosaki, Y., Takayanagi, T., 1999. Measurements of thermal rate constants for the reactions of N(^{2}D,^{2}P) with C$_2$H$_4$ and C$_2$D$_4$ between 225 and 292 K. J. Phys. Chem. A 103, 8650–8656.

Sekine, Y., Imanaka, H., Lebonnois, S., Khare, B.N., Bakes, E.L.O., McKay, C.P., Sugita, S., Matsui, T., 2006. The role of organic haze in the hydrogen budget on Titan. First European Planetary Science Congress 2006, EPSC2006-A-00312.

Sillesen, A., Ratajczak, E., Pagsberg, P., 1993. Kinetics of the reaction $H + C_2H_4 \rightarrow C_2H_5$, $H + C_2H_5 \rightarrow 2CH_3$, $CH_3 + C_2H_5 \rightarrow$ products studied by pulse radiolysis combined with infrared diode lase spectroscopy. Chem. Phys. Lett. 201, 171–177.

Sims, I.R., Queffelec, J.-L., Travers, D., Rowe, B., Herbert, L.B., Karthäuser, J., Smith, I.W.M., 1993. Rate constants for the reactions of CN with hydrocarbons at low and ultra-low temperatures. Chem. Phys. Lett. 211, 461–468.

Slagle, I.R., Gutman, D., Davies, J.W., Pilling, M., 1988. Study of the recombination reaction $CH_3 + CH_3 \rightarrow C_2H_6$. I. Experiment. J. Phys. Chem. 92, 2455–2462.

Smith, G., 2003. Rate theory of methyl recombination at the low temperatures and pressures of planetary atmospheres. Chem. Phys. Lett. 376, 381–388.

Smith, G.R., Strobel, D.F., Broadfoot, A.L., Sandel, B.R., Shemansky, D.E., Holdberg, J.B., 1982. Titan's upper atmosphere: composition and temperature from the EUV solar occultation results. J. Geophys. Res. 87, 1351–1359.

Sugai, H., Yoshida, S., Toyoda, H., 1989. Hydrogen retention and release dynamics of amorphous carbon films exposed to a hydrogen plasma. Appl. Phys. Lett. 54, 1412–1414.

Tanguy, L., Bézard, B., Marten, A., Gautier, D., Gérard, E., Paubert, G., Lecacheux, A., 1990. Stratospheric profile of HCN on Titan from millimeter observations. Icarus 85, 43–57.

Teanby, N.A., and 11 co-authors, 2006. Latitudinal variations of HCN, HC_3N, and C_2N_2 in Titan's stratosphere derived from Cassini CIRS data. Icarus 181, 243–255.

Teslja, A., Nizamov, B., Dagdigian, P.J., 2004. The electronic spectrum of methyleneimine. J. Phys. Chem. A 108, 4433–4439.

Tomasko, M.G., Lemmon, M., Roose, L.R., Smith, P.H., Eibl, A., West, R.A., 1997. Models of the penetration of sunlight into the atmosphere of Titan. ESASP-1177, 345–358.

Tomasko, M.G., and 39 co-workers, 2005. Rain, winds, and haze during the Huygens probe's descent to Titan's surface. Nature doi:10.1038/nature04126.

Toon, O.B., McKay, C.P., GriKth, C.A., Turco, R.P., 1992. A physical model of Titan aerosols. Icarus 95, 24–53.

Toublanc, D., Parisot, J.P., Brillet, J., Gautier, D., Raulin, F., McKay, C.P., 1995. Photochemical modeling of Titan's atmosphere. Icarus 113, 2–26.

Tsang, W., Hampson, R.F., 1986. Chemical kinetic data base for combustion chemistry. Part 1. Methane and related compounds. J. Phys. Chem. Ref. Data 15, 1087–1279.

Vereecken, L., De Groof, P., Peeters, J., 2003. Temperature and pressure dependent product distribution of the addition of CN radicals to C_2H_4. Phys. Chem. Chem. Phys. 5, 5070–5076.

Vervack, R.J., Sandel, B.R., Strobel, D.F., 2004. New perspectives on Titan's upper atmosphere from a reanalysis of the Voyager 1 UVS solar occultations. Icarus 170, 91–112.

Vinatier, S., et al., 2006. Vertical abundance profiles of hydrocarbons in Titan's atmosphere at 15°S and 80°N retrieved from Cassini/CIRS spectra, in press.

Vuitton, V., Yelle, R.V., Anicich, V.G., 2006a. The nitrogen chemistry of Titan's upper atmosphere revealed. Ap. J. 647, L175–L178.

Vuitton, V., Yelle, R.V., Anicich, V.G., 2006b. Detection of complex molecules in Titan's upper atmosphere. DPS meeting, # 38, # 36.03.

Waite Jr., J.H., and 21 co-authors, 2005. Ion neutral mass spectrometry results from the first flyby of Titan. Science 308, 982–986.

Wang, H., Frenklach, M., 1994. Calculations of rate coefficients for the chemically activated reactions of acetylene with vinylic and aromatic radicals. J. Phys. Chem. 98, 1465–1489.

Wilson, E.H., Atreya, S.K., 2003. Chemical sources of haze formation in Titan's atmosphere. Planet. Space Sci. 51, 1017–1033.

Wilson, E.H., Atreya, S.K., 2004. Current state of modeling the photochemistry of Titan's mutually dependent atmosphere and ionosphere. J. Geophys. Res. 109.

Yelle, R.V., 1991. Non-LTE models of Titan's upper atmosphere. Astrophys. J. 383, 380–400.

Yelle, R.V., Waite, J.H., Cravens, T., Ip, W., Kasprzak, W., Ledvina, S., Luhmann, J., Müeller-Wodarg, I., McNutt, R., Niemann, H., de la Haye, V., Borggren, N., 2005. Vertical structure of Titan's atmosphere from INMS observations. Titan Cassini/Huygens meeting: Titan after the Huygens and first Cassini encounters.

Yelle, R.V., Borggren, N., de la Haye, V., Kasprzal, W.T., Niemann, H.B., Müller-Wodarg, I., Waite, J.H., 2006. The vertical structure of Titan's upper atmosphere from the Cassini ion neutral mass spectrometer measurements. Icarus 182, 567–576.

Yu, T., Lin, M.C., Melius, C.F., 1994. Absolute rate constant for the reaction of phenyl radical with acetylene. Int. J. Chem. Kin. 26, 1095–1104.

Yung, Y.L., Allen, M., Pinto, J.P., 1984. Photochemistry of the atmosphere of Titan: comparison between model and observations. Astrophys. J. 55 (Suppl.), 465–506.

Zalicki, P., Ma, Y., Zare, R.N., Wahl, E.H., Dadamio, J.R., Owano, T.G., Kruger, C.H., 1995. Methyl radical measurement by cavity ring-down spectroscopy. Chem. Phys. Lett. 234, 269–274.

Zhu, R.S., Xu, Z.F., Lin, M.C., 2004. *Ab initio* studies of alkyl radical reactions: combination and disproportionation reactions of CH_3 with C_2H_5, and the decomposition of chemically activated C_3H_8. J. Chem. Phys. 120, 6566–6573.